NTNU

Cold Climate Engineering

DTU

# Performance of fully grouted GFRP rock bolt in combined pull and shear

Department of
Wind Energy
Master Report

Mikkel Baastrup Hovgaard

DTU Wind Energy-M-0317

June 2019

**DTU Wind Energy**
Department of Wind Energy

**Author:** Mikkel Baastrup Hovgaard

**Title**: Performance of fully grouted GFRP rock bolt in combined pull and shear

DTU Wind Energy is a department of the Technical University of Denmark with a unique integration of research, education, innovation and public/private sector consulting in the field of wind energy. Our activities develop new

**DTU Wind Energy-M-031717**
**June 2019**

**Project period:**
**January 2019 – June 2019**

**ECTS: 30**

**Education: Master of Science**

**Supervisor:**
Charlie Chunlin Li
**NTNU, Norway**

Lars Pilgaard Mikkelsen
**DTU Wind Energy**

**Remarks:**
This report is submitted as partial fulfillment of the requirements for graduation in the above education at the Technical University of Denmark.

# i Abstract

Glass Fiber Reinforced Polymer (GFRP) rock bolts is gaining attention, as an alternative to steel bolts, for permanent rock support. GFRP holds many advantages for this purpose, including light weight, lower environmental impact and excellent durability characteristics. However, the shear strength of GFRP rock bolts has been proven to be significantly lower than the tensile strength, which raises a concern in combined loading condition. The report has through several experiments defined important parameters and evaluated the performance of a GFRP rock bolt in a combined loading condition. It was found that the strength of the rock bolt at 47° displacement angle was similar to the tensile strength (0°), while in the range of 47° to 72° the strength would drop significantly to a value closer to what was measured in pure shear (90°). Finally an attempt was made, to replicate the obtained results, using numerical modelling. This had limited success, thereby indicating that a more advanced model is required to properly simulate the behaviour of a GFRP rock bolt.

# ii Preface

This project is the masters thesis in the joint masters program Cold Climate Enginnering: Land Track, between the Norwegian University of Science and Technology (NTNU) and the Technical University Of Denmark (DTU).

I would like to thank everyone who has assisted with the experiments throughout the project.

From NTNU department of geoscience and petroleum:

- Gunnar Vistnes - For assisting with full scale bolt tests.
- Jon Runar Drotninghaug - For assisting with full scale bolt tests.

From DTU department of energy:

- Anette Pedersen - For preparing microscope specimens and performing the matrix burn-off method.
- Søren Fæster - For assisting with SEM microscopy.
- Anthony Fraisse - For performing uniaxial tensile tests.
- Christen Malte Markussen - For assisting with optical microscopy.

Finally i wish to thank my family and my girlfriend Danielle Hallé for support throughout the project.

# Contents

# 1 Introduction

Glass Fiber Reinforced Polymer (GFRP) refers to a group of composite materials that consists of glass fibers bonded together with a polymer (Thomas, 2018). Examples of these polymers are polyester, vinylester and epoxy (Barbero, 2017).

For rock support GFRP has primarily been used as temporary support, in mining for rock that would later be removed and crushed, because GFRP bolts can be crushed with the rock, without damaging the equipment (Stjern, 1995).

According to Thomas (2018) the advantages of using GFRP for permanent rock support are many, compared to steel, these include light weight, reduced manual handling impact on workers, lower environmental impact and excellent durability characteristics. However, the shear strength of GFRP rock bolts has been proven to be significantly lower than the tensile strength and the strength in a combined loading condition is not known, which can complicate the use in many situations.

Figure 1.1: GFRP rock bolt with centimetre scale

## 1.1 Loading Condition

A scenario where a rock bolt is subjected to a combined tension and shear load is, when supporting a wedge block sliding from a rock wall, as illustrated in Figure 1.2. In this scenario the bolt is installed perpendicular to the surface wall through a wedge block and into stable rock mass. The joint between the wedge block and the stable rock mass defines the shearing plane, which runs at an angle to the rock bolt. The resulting force that acts on the bolt relative to the bolt direction is therefore a combination of tensile and shear forces.

Rock bolts are not the only contributor to shear resistance of a joint, which has been described by Bjurstrom (1974) in Eq. 1.1.

$$F = F_S + F_d + F_t \tag{1.1}$$

Where $= F_S$ is the joint shear resistance, $F_d$ is the shear resistance of the bolt and $F_t$ is the increased shear resistance in the joint due to axial load in the bolt. The experiments and simulations carried out for this report are primarily focused on the shear resistance of the bolt $F_d$, and are therefore designed to exclude any contributions from the joint.

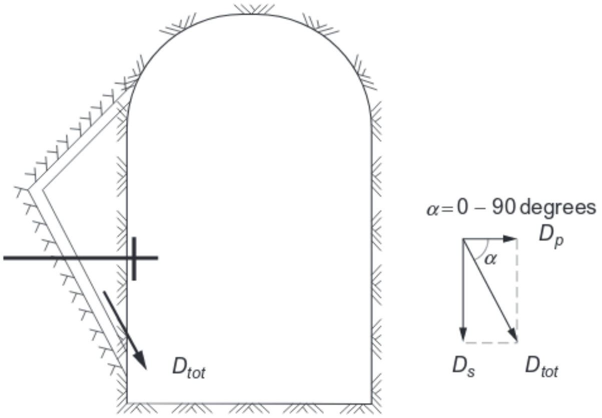

Figure 1.2: Wedge block in wall (Li, 2017)

## 1.2 Description of the rock bolt

The particular rock bolt investigated in this report is made from a Glass Fiber Reinforced Polymer (GFRP), using E-glass and vinylester. The bolt is a pultruded thread bar with rounded threading as shown in Figure 1.1, the dimensions of the bolt are given in Table 1.1.

A nut and face plate can be installed on the bolt as shown in Figure 1.3. This allows the bolt to establish contact with the wall surface and to hold surface retaining support. The area of contact between the nut and face plate is dome shaped, allowing the face plate to tilt and gain better contact with an uneven rock surface.

Table 1.1: Dimensions of the GFRP bolt

| Outer Diameter | Pitch Diameter | Root width | Pitch |
|---|---|---|---|
| 25 mm | 24 mm | 2 mm | 10 mm |

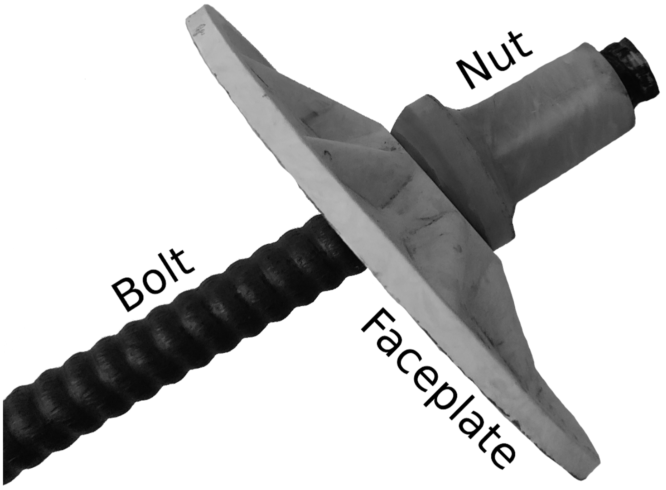

Figure 1.3: GFRP bolt with nut and faceplate

## 1.3 Aim of project

The aim of the project is to investigate the performance of the rock bolt in a combined loading condition. This is investigated through a series of experiments, micro mechanics and numerical modelling, where the main questions are:

- What are the mechanical properties of the bolt and how are they established?
- What is the ultimate load and displacement of the bolt at different displacement angles?
- How are stresses distributed within the bolt and how do they contribute to the failure of the bolt?

These questions are answered throughout the report with the following structure:
Chapter 2 establishes the relevant mechanical parameters for the bolt.
Chapter 3 investigates the performance of the rock bolt through full scale laboratory testing.
Chapter 4 Uses numerical modelling to replicate the full scale experiment, with data obtained from Chapter 2 and 3 to investigate the stresses in the bolt.

# 2 Mechanical Properties

## 2.1 Introduction

An unidirectional fiber composite can be described elastically as an orthotropic material, which has 3 planes of symmetry, one perpendicular to the fibers and the remaining two is any pair, parallel to the fiber direction An orthotropic material is defined by: $E_1$, $E_2$, $E_3$, $G_{12}$, $G_{13}$ ,$G_{23}$, $v_{12}$ ,$v_{13}$, $v_{23}$, where E is the elastic modulus, $G$ the shear modulus and $v$ is Poisson's ratio. The numbering indicates direction or plane as shown in Figure 2.1, where 1 is the fiber direction.

If the unidirectional fibers are randomly distributed throughout the cross section, the material can be regarded as transverse isotropic, of which the elastic parameters can be simplified from an orthrotropic material to: $E_1$, $E_2$, $G_{12}$, $G_{23}$, $v_{12}$ and ,$v_{23}$, with $E_2 = E_3$, $v_{13} = v_{12}$, and $G_{13} = G_{12}$ (Barbero, 2017).

The aim of this chapter is to define the mechanical properties necessary to describe the behaviour of a GFRP rock bolt. This is done based on a combination of micro mechanics and experimental work, including microscopy, the matrix burn-off method and uniaxial tensile testing.

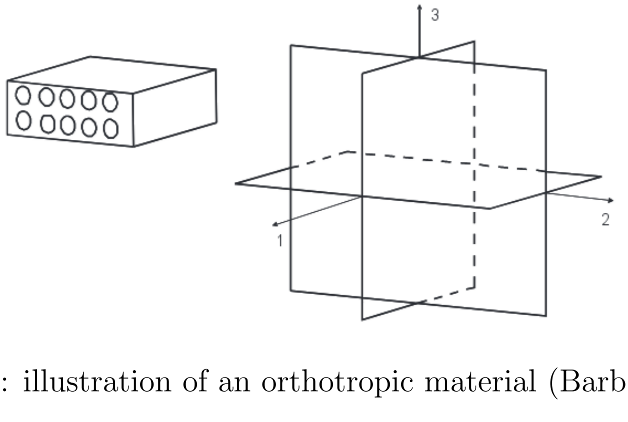

Figure 2.1: illustration of an orthotropic material (Barbero, 2017)

## 2.2 Elastic properties

The material of the rock bolt is a composite of E-glass fiber and a vinylester. Individually these materials are considered isotropic, where the elastic parameters $E$, $G$ and $v$ are related through Eq. 2.1

$$E = 2G(1 + v) \tag{2.1}$$

and the bulk modulus K can be calculated from

$$K = \frac{E}{3(1 - 2v)} \tag{2.2}$$

The elastic parameters of a composite are more difficult to determine and require different approaches depending on the direction and plane of which the parameters are described.

Material parameters for E-glass and vinylester used throughout this chapter are given in Table 2.1. It is noted that the parameters are from the literature and the values might deviate from the ones used in the rock bolt, but they are expected to be fairly similar.

Table 2.1: Material parameters from Barbero (2017)

| | $E$ [GPa] | $v$ [-] | $\sigma_t$ [MPa] | $\sigma_c$ [MPa] | $\tau$ [MPa] | $\rho$ [kg/$m^3$] |
|---|---|---|---|---|---|---|
| Vinylester | 3.4 | 0.38 | 82.7 | 117.1 | 82.7 | 1120 |
| E-glass | 72.35 | 0.22 | 3450 | | | 2600 |

### 2.2.1 Axial and Transverse stiffness

The axial stiffness of a composite material is considered to be a weighted average of the individual components. A model used to represent a composite is the slab model, which considers each component as a slab of homogeneous material as seen in Figure 2.2.

The slab model represents an unidirectional fiber composite very well in the fiber direction, which leads $E_1$ to be a weighted average of the individual components, also referred to as rule of mixtures.

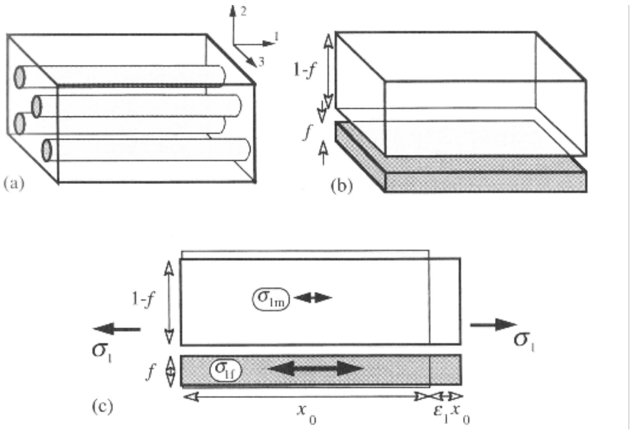

Figure 2.2: Illustration on how a composite can be simplified to a slab model (Hull and Clyne, 1996)

$$E_1 = (1 - V_f)E_{\mathrm{m}} + V_f E_{\mathrm{f}} \tag{2.3}$$

Where $V_f$ is the fiber volume fraction $E_{\mathrm{m}}$ is the matrix stiffness and $E_{\mathrm{f}}$ is the fiber stiffness. Minor deviations are expected if $v$ of the separate components are not equal. (Hull and Clyne, 1996)

The transverse stiffness $E_2$ is not very well represented with the slab model. A common approach to estimate $E_2$ is through a semi-empirical equation from Halpin and Tsai (1967) in Eq. 2.4

$$E_2 = \frac{E_{\mathrm{m}}(1 + \xi\eta V_f)}{(1 - \eta V_f)} \tag{2.4}$$

Where

$$\eta = \frac{\left(\frac{E_{\mathrm{f}}}{E_{\mathrm{m}}} - 1\right)}{\left(\frac{E_{\mathrm{f}}}{E_{\mathrm{m}}} - \xi\right)} \tag{2.5}$$

and $\xi$ is a correction factor, which is suggested to 2.

### 2.2.2 Poisson's Ratio

Poisson's ratio $v_{ij}$ describes contraction in the $j$ direction when stress is applied in the $i$ direction. The relevant Poisson's ratios for a transverse isotropic fiber composite is shown in Figure 2.3

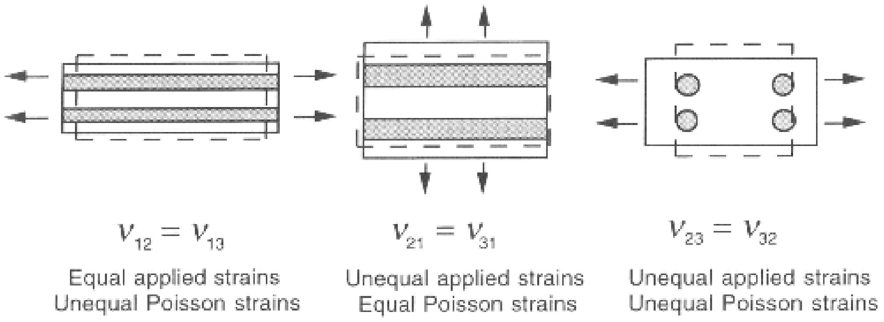

Figure 2.3: Poisson's ratio in three directions (Hull and Clyne, 1996)

Poisson's ratio for $v_{12}$ can be estimated using rule of mixtures as shown in Eq. 2.6

$$v_{12} = (1 - V_f)v_{\mathrm{m}} + V_f v_{\mathrm{f}} \tag{2.6}$$

According to Hull and Clyne (1996) $v_{23}$ may be obtained by considering the total volume change experienced by the material, which leads to Eq. 2.7

$$v_{23} = 1 - v_{21} - \frac{E_2}{3K} \tag{2.7}$$

Where

$$v_{21} = \frac{E_2 v_{12}}{E_1} \tag{2.8}$$

and

$$K = \left[\frac{f}{K_f} + \frac{1-f}{K_m}\right]^{-1} \tag{2.9}$$

### 2.2.3 Shear Modulus

The in-plane shear modulus $G_{12}$ is not well represented with the slab model. Figure 2.4 shows the difference between the behavior of an actual sample and the slab model, where the slab model can be divided into an equal stress and an equal strain model. According to Hull and Clyne (1996) the rule of mixtures, which corresponds to the equal strain condition, will give a gross over estimation of $G_{12}$, while the inverse rule of mixtures is a significant underestimate. The suggested way of calculating $G_{12}$ is therefore by using the semi-empirical expression of Halpin and Tsai (1967) in Eq. 2.10

$$G_{12} = \frac{G_{\mathrm{m}}(1 + \xi\eta f)}{(1 - \eta f)} \tag{2.10}$$

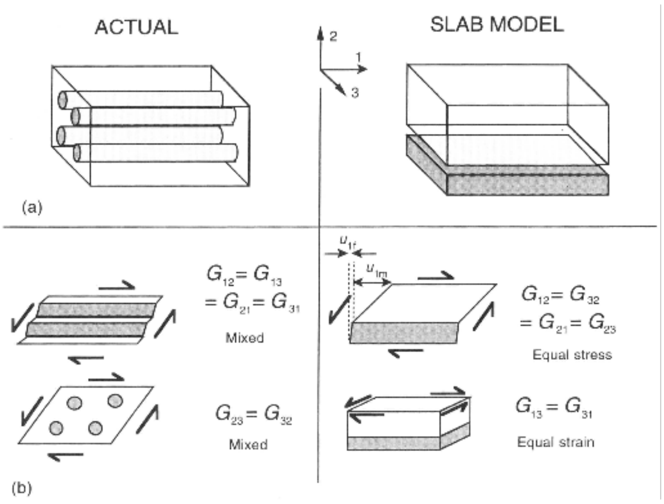

Figure 2.4: Difference between the actual shape and the slab model when subjected to shear (Hull and Clyne, 1996)

Where

$$\eta = \frac{\left(\frac{G_\mathrm{f}}{G_\mathrm{m}} - 1\right)}{\left(\frac{G_\mathrm{f}}{G_\mathrm{m}} - \xi\right)} \tag{2.11}$$

and $\xi$ is a correction factor, with a recommended value of 2 for round fibers.

For transverse isotropic materials $G_{23}$ is given by Eq. 2.12 (Barbero, 2017)

$$G_{23} = \frac{1}{2} E_2/(1 + v_{23}) \tag{2.12}$$

## 2.3 Optical Microscopy

The rock bolt was investigated through an optical microscope, to get an overview of the cross section perpendicular and parallel to the fibers.

### 2.3.1 Method

The optical microscope used for this project was a Leica DMI5000M set to 50x magnification, equipped with a Leica DMC2900 camera with a image resolution of 2048x1536 pixels. The microscope setup is shown in Figure 2.5. It is equipped with a mounting plate that can move in the xy plane and be controlled from a computer, which allows the user to capture images in a controlled grid to cover the whole surface of a specimen. A custom specimen holder was 3D printed for this experiment.

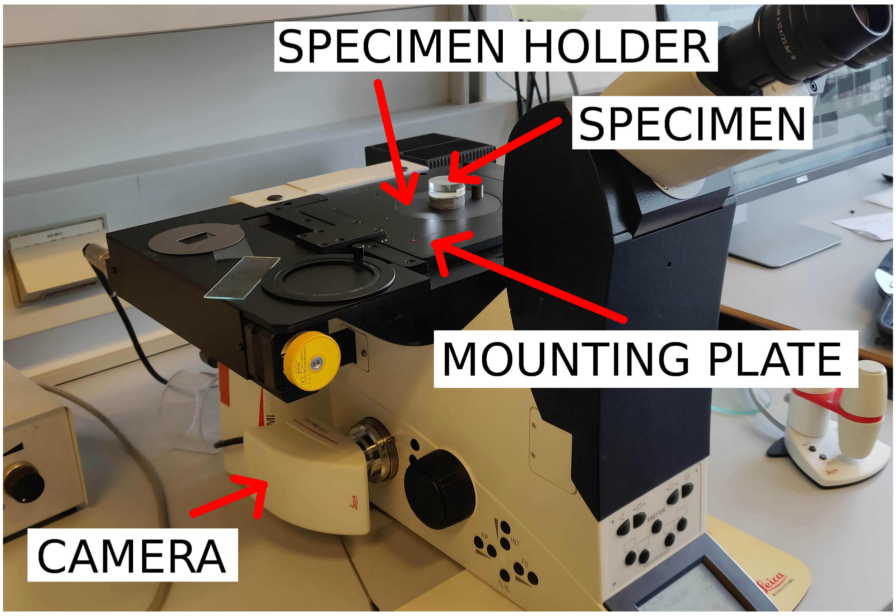

Figure 2.5: Setup of the optical microscope

### 2.3.2 Preparation of specimens

Six specimens were prepared by cutting off small sections of the bolt and casting them into a clear resin, four were cut perpendicular and two parallel to the fiber

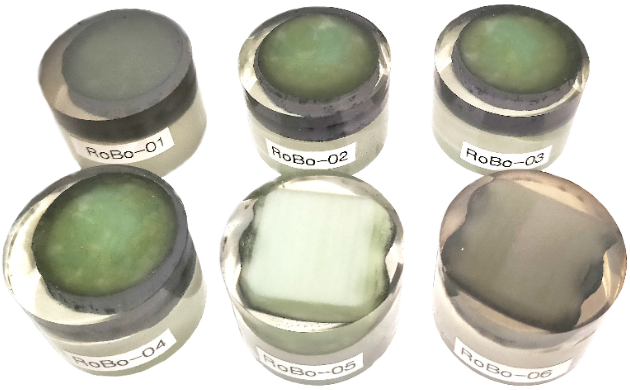

Figure 2.6: Image of the specimens used for microscopy

direction. The specimens were then polished on the cut side, to ensure a smooth surface with no resin residuals. RoBo-01 and RoBo-06, were prepared for the SEM, described in section 2.4, by coating the surface, with a few nanometer thick carbon layer, to make it conductive.

### 2.3.3 Running the test

The microscope was set to take photos of the specimens in an 18x27 image array, which were then stitched together, using PTGui, to create high resolution panoramas image of the specimens.

### 2.3.4 Data and Data Treatment

The data obtained with the optical microscope consists of high resolution stitched images of the surface of specimen: RoBo-01, RoBo-02, RoBo-03, RoBo-04, and RoBo-05. Where images of RoBo-02 and RoBo-05 are reported in Figure 2.8 and 2.9, representing a cross section of the bolt perpendicular and parallel to the fibers.

A close up can be seen in Figure 2.7, where the glass fibers appear as light grey features that are circular when the viewed plane is perpendicular to the fiber direction.

The cross section of RoBo02 is displayed in Figure 2.8 where it is evident that the fibers are not evenly distributed throughout the cross section. From visual inspection it appears that the bolt has a core with relatively high fiber volume

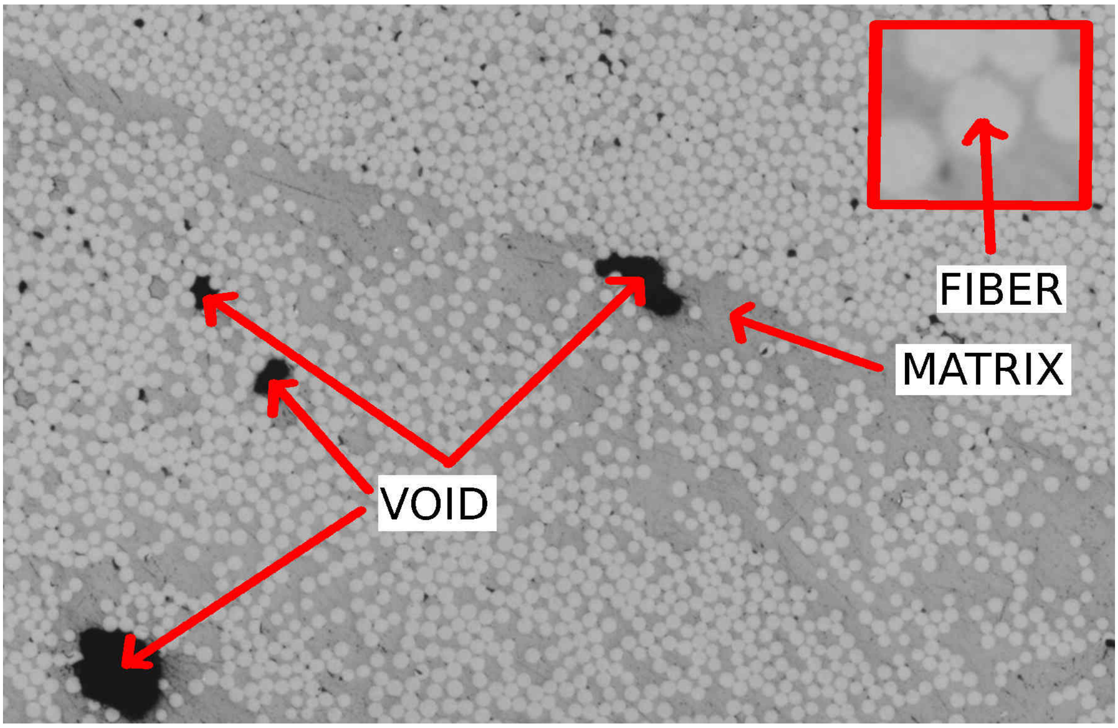

Figure 2.7

fraction and a section along the edge of the bolt with a lower fiber volume fraction. When comparing to the image of RoBo-05, in Figure 2.9, it is clear that the section with lower fiber volume fraction is at the crest of the thread.

The images of Robo-01, Robo-02, Robo-03 and Robo-04 were analyzed in the Geographic Information Systems software QGIS. The software is designed for geographic data, but works equally well for analyzing images on a pixel level.

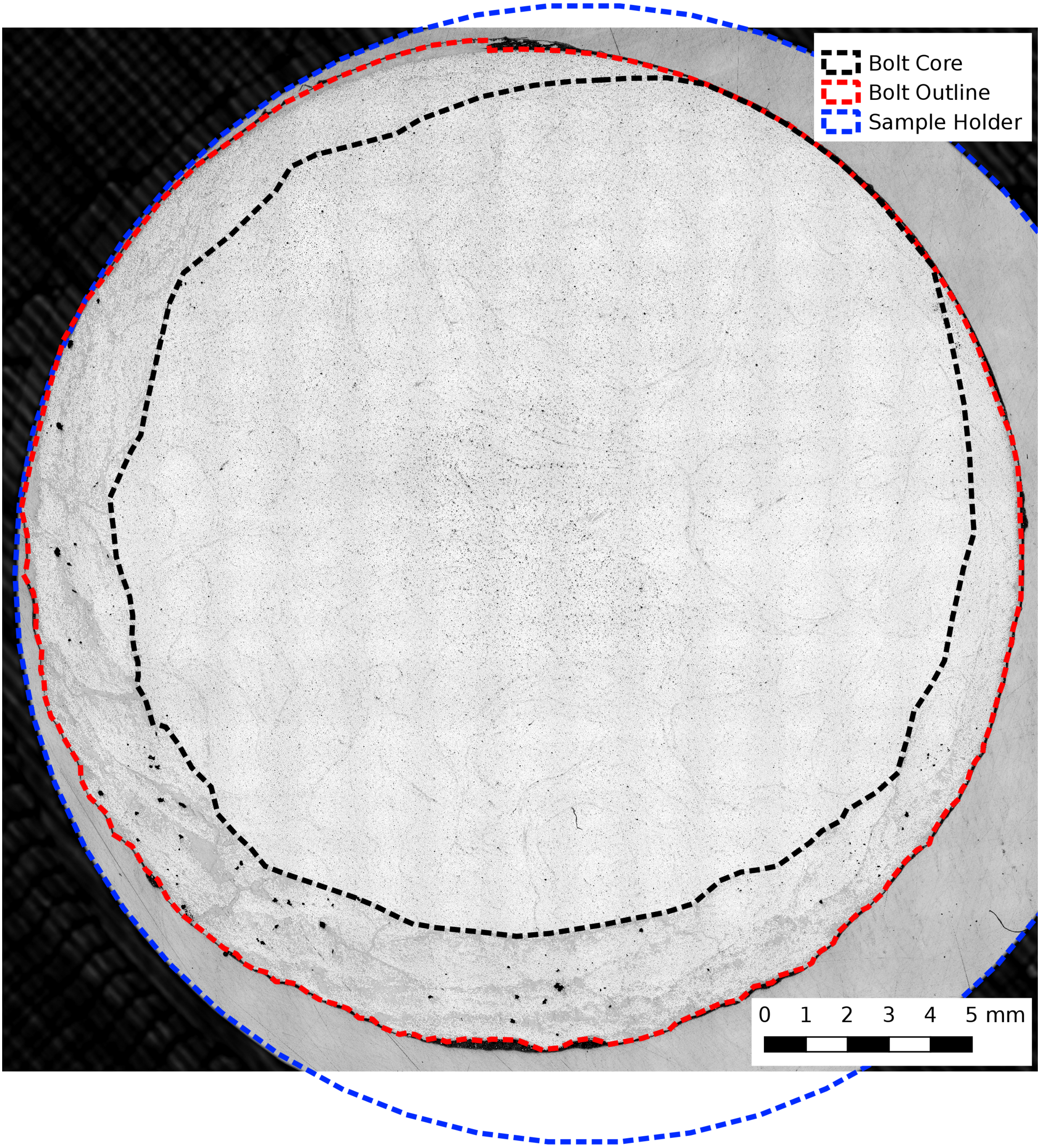

Figure 2.8: Stitched image of RoBo_02

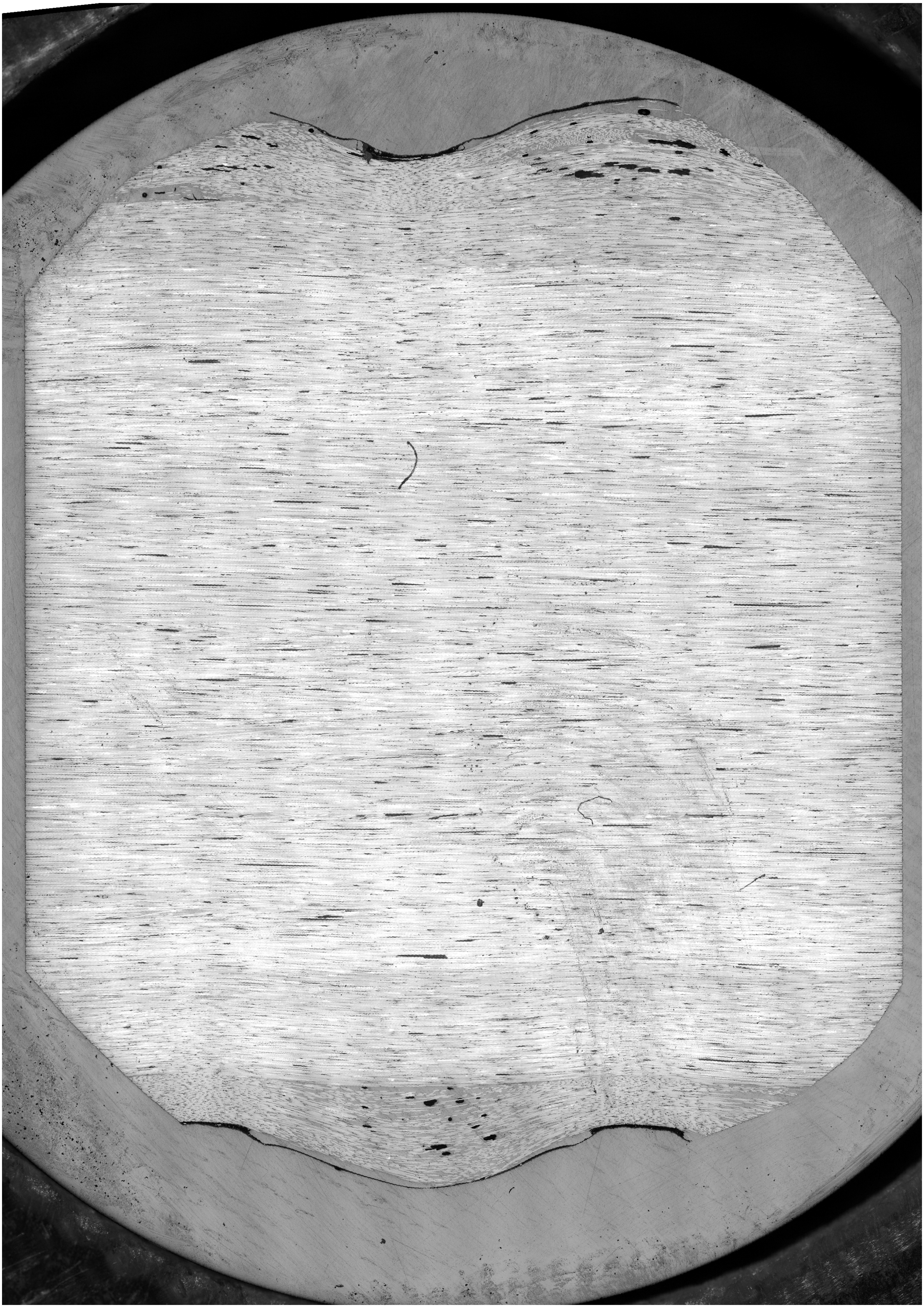

Figure 2.9: Stitched image of RoBo_05

Table 2.2: Radius of circle fitted to the specimen holder

| Specimen | $r_{\text{holder},1}$ [pixel] | $r_{\text{holder},2}$ [pixel] | mean [pixel] |
|---|---|---|---|
| *RoBo*_01 | 13792 | 13794 | 13793 |
| *RoBo*_02 | 13633 | 13634 | 13634 |
| *RoBo*_03 | 14184 | 14139 | 14162 |
| *RoBo*_04 | 13893 | 13861 | 13877 |

Table 2.3: Conversion matrix

| | RoBo-01 | RoBo-02 | RoBo-03 | RoBo-04 |
|---|---|---|---|---|
| RoBo-01 | 1.000 | 0.988 | 1.027 | 1.006 |
| RoBo-02 | 1.012 | 1.000 | 1.039 | 1.018 |
| RoBo-03 | 0.974 | 0.963 | 1.000 | 0.980 |
| RoBo-04 | 0.994 | 0.982 | 1.020 | 1.000 |

### Correcting pixel size

The sample holder used on the optical microscope caused the specimen to sit lower than what the microscope was calibrated for, which caused the pixel size for the images to be unknown. The procedure used to find the correct pixel size is described below.

A circle was fitted to the sample holder twice to insure the quality of the fit. The radius of the sample holder, in Table 2.2, were then compared to each other, to check if the images had similar pixel sizes, where they were found not to match. A conversion matrix was therefore established in Table 2.3, to show the found relationship between the images. In example: A feature in RoBo-03 is 1.02 times larger in RoBo-04.

The pixel sizes then had to be connected to a physical unit, for which, in total 4 pairs of features were selected on the specimens of where 1 pair was found on RoBo-02, 2 pairs on RoBo-03 and 1 pair on RoBo-04. The distance between each feature pair was measured physically with calipers and on the image using QGIS. See Table 2.4.

The relationship between $l_{\text{physical}}$ and $l_{\text{image}}$ for each feature pair was converted to each specimen, using the conversion matrix in Table 2.3. Finally, the best estimate for a pixel size of each image was found as the average of the converted relationships between $l_{\text{physical}}$ and $l_{\text{image}}$, shown in Table 2.5.

Table 2.4: Distance between feature pairs

| $feature$ | $l_{physical}$ [mm] | $l_{image}$ [pixel $10^3$] | $\frac{l_{physical}}{l_{image}}$ [-] |
|---|---|---|---|
| $ft_2$ | 23.5 | 23.87 | 0.985 |
| $ft_{3.1}$ | 22.8 | 24.01 | 0.950 |
| $ft_{3.2}$ | 21.8 | 22.48 | 0.970 |
| $ft_4$ | 23.5 | 24.02 | 0.979 |

Table 2.5: Pixel size for each image in $\frac{\mathrm{m}}{pixel}10^{-6}$

| Image | $ft_2$ | $ft_{3.1}$ | $ft_{3.2}$ | $ft_4$ | $mean$ |
|---|---|---|---|---|---|
| RoBo-01 | 0.973 | 0.975 | 0.996 | 0.985 | 0.982 |
| RoBo-02 | 0.985 | 0.986 | 1.007 | 0.996 | 0.994 |
| RoBo-03 | 0.948 | 0.950 | 0.970 | 0.959 | 0.957 |
| RoBo-04 | 0.967 | 0.969 | 0.990 | 0.979 | 0.976 |

### Cross sectional area

With the pixel size established in Table 2.5 the area of the thread and core can be estimated by outlining the bolt and core with polygons in QGIS as shown in Figure 2.8. The areas of the polygons are given in Table 2.6. The bolt was partly covered by the sample holder for RoBo_3, so the bolt outline could not be drawn.

The measured areas are finally converted to mm$^2$ in Table 2.7, where the thread area is found from Eq. 2.13

$$A_{\text{thread}} = A_{\text{bolt}} - A_{\text{core}} \tag{2.13}$$

Table 2.6: Area of polygons measured in pixels

| Specimen | $A_{\text{core}}$ | $A_{\text{bolt}}$ |
|---|---|---|
| *RoBo*_01 | 352865142 | 456654792 |
| *RoBo*_02 | 334593804 | 449418231 |
| *RoBo*_03 | 361956159 | - |
| *RoBo*_04 | 360569555 | 464854048 |

Table 2.7: Area of bolt sections in [$mm^2$] and by volume fraction [-]

| Specimen<br>Specimen | $A_{core}$<br>[$mm^2$] | $A_{thread}$<br>[$mm^2$] | $A_{bolt}$<br>[$mm^2$] | $V_{core}$<br>[-] | $V_{thread}$<br>[-] |
|---|---|---|---|---|---|
| *RoBo*_01 | 340.35 | 100.11 | 440.46 | 0.773 | 0.227 |
| *RoBo*_02 | 330.31 | 113.35 | 443.66 | 0.745 | 0.255 |
| *RoBo*_03 | 331.19 | 111.16 | 442.35 | 0.749 | 0.251 |
| *RoBo*_04 | 343.56 | 99.37 | 442.93 | 0.776 | 0.224 |
| *mean* | 336.35 | 106.00 | 442.35 | 0.760 | 0.240 |
| *sd* | 6.61 | 7.29 | 1.37 | 0.02 | 0.02 |

### 2.3.5 Results and Discussion

The optical microscope analysis found that the cross sectional area of the bolt is divided into two areas, with different characteristics. One part described as the core with a relatively high fiber volume fraction, and a thread area with a lower fiber volume fraction. The described areas are defined as shown in Figure 2.8 and the found areas are given in Table 2.7.

No attempt was made to estimate the fiber volume fraction from optical microscopy. This has been done, using Scanning Electron Microscopy in section 2.4 and from the matrix burn-off method in section 2.5

Despite using the same sample holder for RoBo_01 through RoBo_04 the images appears to have different pixel sizes, with almost 4% difference between RoBo_02 and RoBo_03. This is not believed to be related to inaccurate circle fitting, since the circles could be independently fitted with high accuracy.

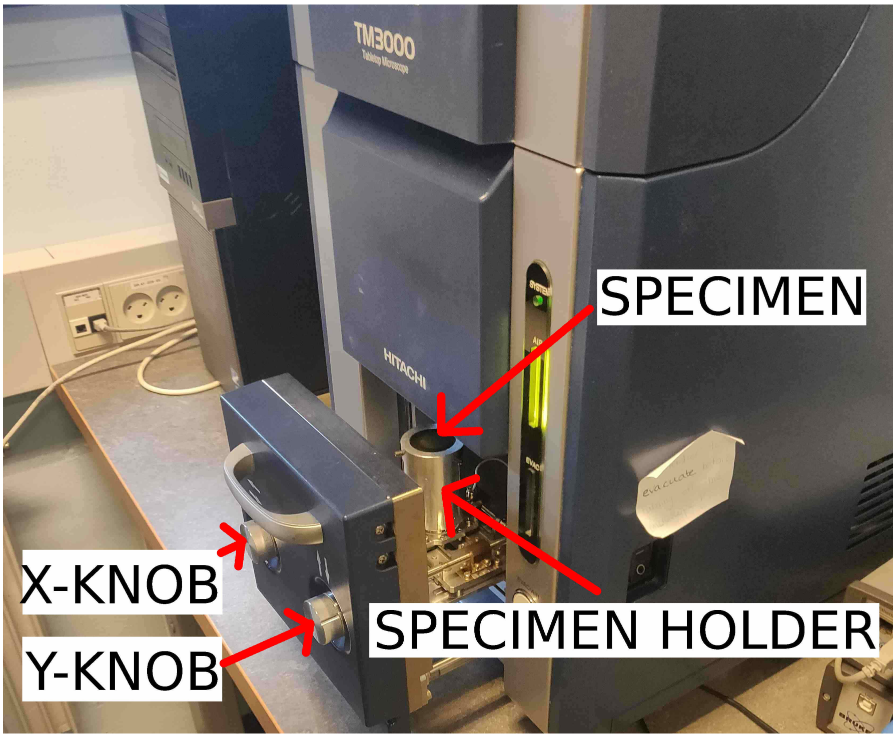

Figure 2.10

## 2.4 Scanning Electron Microscopy

A Scanning Electron Microscope (SEM) generates images by scanning an electron beam of high energy on the sample surface. This was used to determine the fiber volume fraction of the rock bolt.

### 2.4.1 Method

The SEM used for this project is a HITACHI TM3000 set to 200x magnification with a resolution of 1280x960 pixels. The preparation of specimens is described in section 2.3.2 where specimen RoBo_01 was used for the SEM analysis.

The setup is shown in Figure 2.10 The microscope allows for the sample to be moved in the XY plane, by manually turning the indicated knobs, but does not offer any position tracking, which makes it difficult to create a stitched panorama of the whole surface as it was done with the optical microscope in section 2.3. Images were therefore taken in different areas of the core and thread, based on a

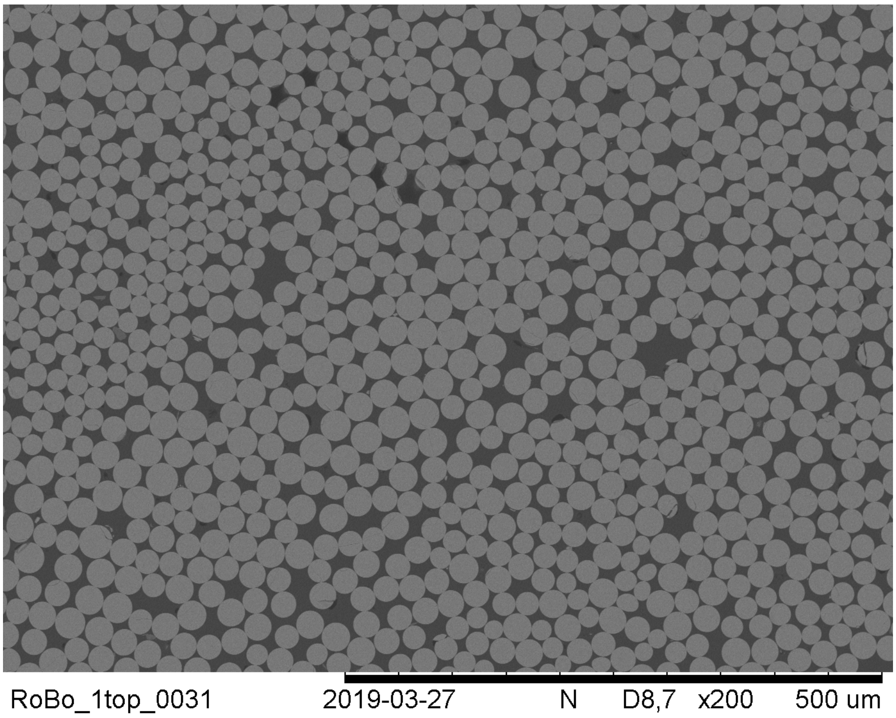

Figure 2.11: Example of SEM images from the bolt core

panorama image of RoBo_01 from the optical microscope similar to the image of RoBo_02 in Figure 2.8.

### 2.4.2 Data and Data Treatment

In total 50 images were taken, of where 29 were from the core and 21 from the thread area. The images taken are similar to the one shown in Figure 2.11, where the lighter circles indicates fibers.

Histograms, showing the pixel values for the SEM image in Figure 2.11 and the optical image in Figure 2.7 are compared in Figure 2.12.

It is evident that the pixels values from SEM are much better separated than from the optical image. This indicates a more distinct transition between fiber and matrix, which is also visible in the individual images.

Based on this distinct transition it is easy to estimate the fiber volume fraction in a SEM image, by simply counting the pixels that represents fibers.

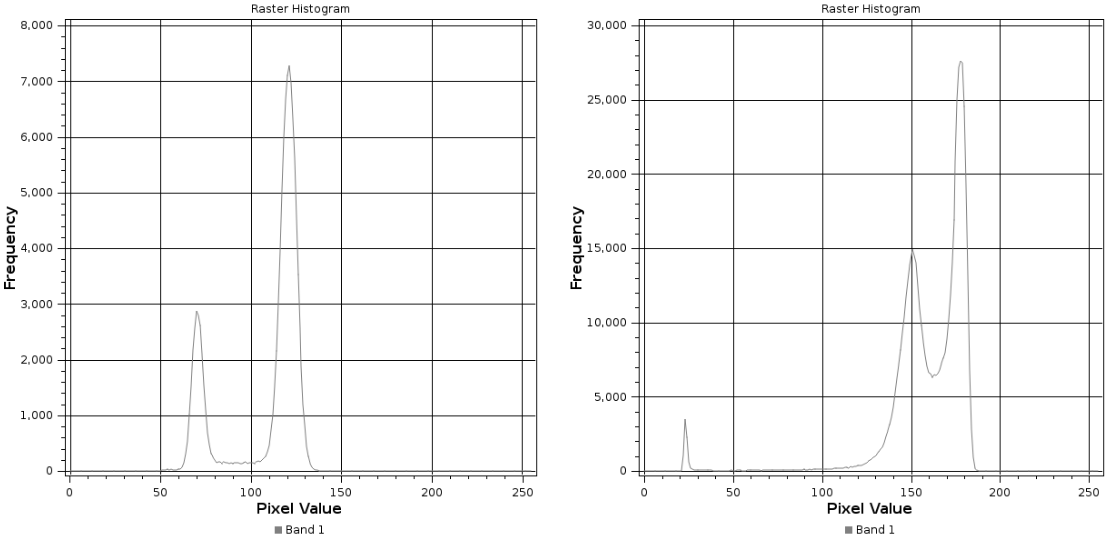

(a) Pixelvalues for SEM image in Figure 2.11

(b) Pixelvalues for optical microscope image in Figure 2.7

Figure 2.12

This is done using a Python script to binarize the images based on a threshold pixel value, automatically selected in between the two peaks, summing the pixel values in the image and dividing by the total amount of pixels as shown in Eq. 2.14

$$V_{\mathrm{f}} = \frac{n_{\mathrm{pixels,f}}}{n_{\mathrm{pixels,total}}} \tag{2.14}$$

The found values for $V_{\mathrm{f}}$ for each image is displayed in a histogram in Figure 2.13, where it is shown that the values for the core are more consistent than the ones for the thread. The mean value for each area is reported in Table 2.8

The fiber volume fraction of the bolt $V_{\mathrm{fbolt}}$ can then be found as a weighted average in Eq 2.15, based on the thread and core fraction $V_{\mathrm{thread}}$ and $V_{\mathrm{core}}$ of the cross sectional area from Table 2.7.

$$V_{\mathrm{fbolt}} = V_{\mathrm{fcore}}V_{\mathrm{core}} + V_{\mathrm{fthread}}V_{\mathrm{thread}} \tag{2.15}$$

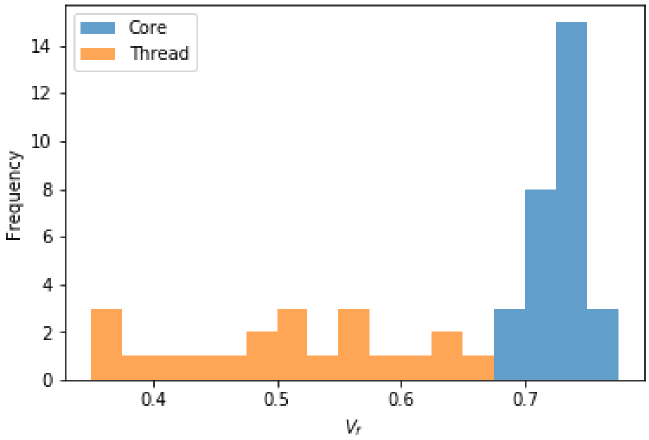

Figure 2.13: Frequency of measured fiber volume fractions

### 2.4.3 Results

The fiber volume fractions, for the core and thread, were successfully found through SEM analysis and reported in Table 2.8.

### 2.4.4 Discussion

This method completely ignores voids, which will be counted as matrix. The void percentage is however assumed to be very low based on visual inspection of the optical images from section 2.3.

Table 2.8

| | $V_{\mathrm{f,core}}$ | $V_{\mathrm{f,thread}}$ | $V_{\mathrm{f,bolt}}$ |
|---|---|---|---|
| $V_{\mathrm{f}}$ | 0.728 | 0.508 | 0.675 |
| $sd$ | 0.019 | 0.091 | 0.036 |

## 2.5 Matrix Burn-off Method

The matrix burn-off method is a way to determine the fiber volume fraction $v_\mathrm{f}$, matrix volume fraction $V_\mathrm{m}$ and the porosity (voids) $V_\mathrm{p}$ x of a composite, from burning off the matrix. The experiment follows the procedure described by Beauson et al. (2019).

### 2.5.1 Method

Five slices of the rock bolt were cut off and dried in a vacuum over night. The mass of each sample were then measured and then measured again while submerged in water, with no contact to the beaker, as shown in Figure 2.14 The samples were then placed in crucibles and burned at 650°C for 18 hours. The crucibles containing the burned samples were then cooled in a desiccator and weighed when they had reached room temperature.

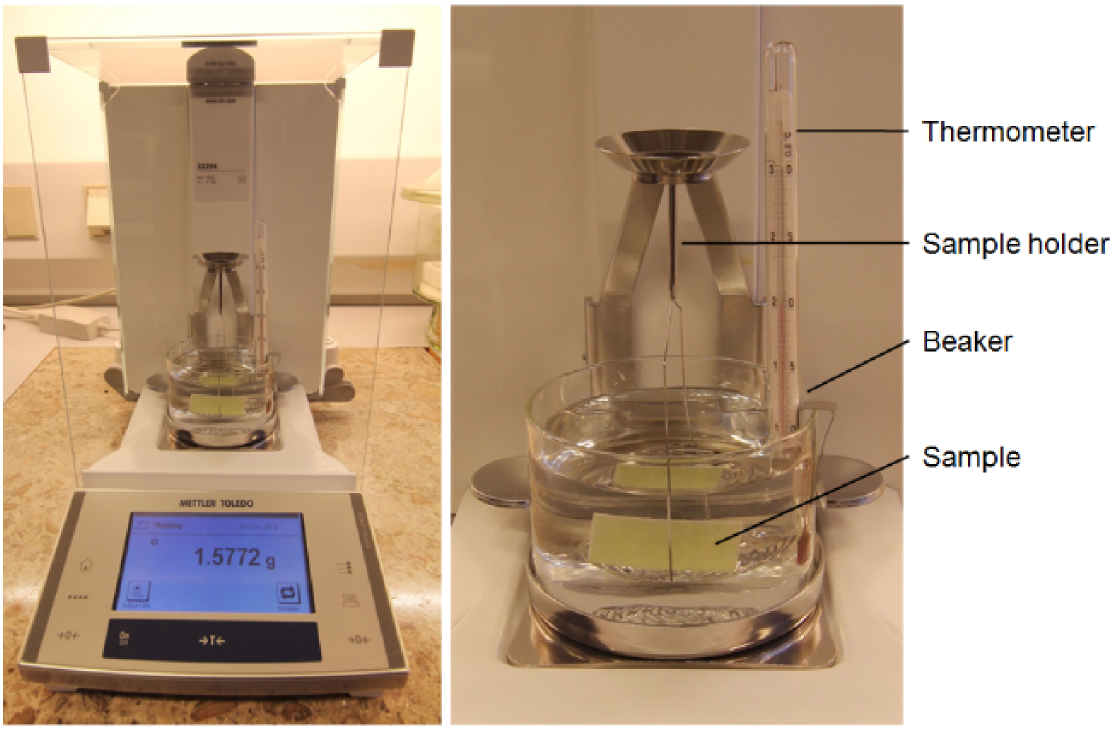

Figure 2.14: Setup for weighing a specimen submergered in water, while avoiding contact with the beaker (Beauson et al., 2019)

Table 2.9: Measured values from the matrix burn-off method

| Specimen | $m_{sample}$ [g] | $T_{water}$ [°C] | $m_{sample,inwater}$ [g] | $crucible_{empty}$ [g] | $crucible_{f}$ [g] |
|---|---|---|---|---|---|
| 1 | 2.7886 | 21.8 | 1.4828 | 23.0500 | 25.3464 |
| 2 | 2.8630 | 21.8 | 1.5117 | 20.8858 | 23.2406 |
| 3 | 2.8344 | 21.8 | 1.5017 | 22.1811 | 24.5234 |
| 4 | 2.6887 | 21.8 | 1.4244 | 22.9874 | 25.2084 |
| 5 | 2.8332 | 21.8 | 1.4983 | 22.8644 | 25.1952 |

### 2.5.2 Data and Data Treatment

The measured values for each specimen are given in Table 2.9.

The fiber volume fraction $V_\mathrm{f}$, matrix volume fraction $V_\mathrm{m}$ and porosity $V_\mathrm{p}$ are found from Eq. 2.16 through 2.18. The used values for $\rho_\mathrm{f}$ and $\rho_\mathrm{m}$ are taken from literature in Table 2.1.

$$V_\mathrm{f} = \frac{\rho_{composite} M_\mathrm{f}}{\rho_\mathrm{f}} \tag{2.16}$$

$$V_\mathrm{m} = \frac{\rho_{composite} M_\mathrm{m}}{\rho_{matrix}} \tag{2.17}$$

$$V_\mathrm{p} = V_\mathrm{m} - V_\mathrm{f} \tag{2.18}$$

Where $M_f$ and $M_m$ are the fiber and matrix weight fraction given by Eq. 2.19 and Eq. 2.20.

$$M_\mathrm{f} = \frac{m_f}{m_{sample}} \tag{2.19}$$

$$M_\mathrm{m} = 1 - M_\mathrm{f} \tag{2.20}$$

$\rho_{composite}$ refers to the density of the specimen, given by Eq. 2.21 and $m_\mathrm{f}$ is the weight of the fibers.

$$\rho_{composite} = \frac{m_{sample} - \rho_{water}}{m_{sample} - m_{sample,inwater}} \tag{2.21}$$

$$m_\mathrm{f} = m_{crucible,\mathrm{f}} - m_{crucible,empty} \tag{2.22}$$

The density of water $\rho_{water}$ is based on the temperature $T_{water}$, calculated with Eq. 2.23

$$\rho_{water} = \left(1 - \frac{49.2539}{1000000}\right) + \frac{T_{water}}{100\left(0.004514 - \frac{T_{water}}{100\left(0.07299 - \frac{T_{water}}{100 \cdot 0.033738}\right)}\right)} \tag{2.23}$$

### 2.5.3 Results

The results from the experiment are shown in Table 2.10 calculated with Eq. 2.16 through 2.23 with the measured values in Table 2.9, and using $\rho_f$ and $\rho_m$ from Table 2.1.

### 2.5.4 Discussion

The results in Table 2.10 shows that the porosity $V_p$ has a negative value, which is physically impossible. This is likely caused by wrong estimates of the matrix density $\rho_m$, which might have a different composition and density than the one taken from the literature.

Looking at the burned specimens in Figure 2.15 it can be seen that they have a slightly green tint, which might be a result of the matrix not being completely burned off, indicating that the matrix is resistant to heat.

However, unburnt matrix will cause a higher value for $V_f$ $V_m$ and $V_p$ which is not believed to be the case for $V_f$ since there is good agreement with the results obtained from microscopy.

Table 2.10: Calculated results from the matrix burn-off method

| Specimen | $\rho_{composite}$ [kg/m$^3$] | $M_f$ [-] | $M_m$ [-] | $V_f$ [-] | $V_m$ [-] | $V_p$ [-] |
|---|---|---|---|---|---|---|
| 1 | 2131 | 0.823 | 0.177 | 0.675 | 0.336 | -0.011 |
| 2 | 2114 | 0.822 | 0.178 | 0.669 | 0.335 | -0.004 |
| 3 | 2122 | 0.826 | 0.174 | 0.675 | 0.329 | -0.003 |
| 4 | 2122 | 0.826 | 0.174 | 0.674 | 0.330 | -0.004 |
| 5 | 2118 | 0.823 | 0.177 | 0.670 | 0.335 | -0.005 |
| mean | 2121 | 0.824 | 0.176 | 0.672 | 0.333 | -0.005 |
| sd | 6 | 0.002 | 0.002 | 0.003 | 0.003 | 0.003 |

Figure 2.15: Burnt GFRP specimens

## 2.6 Tensile Testing

The most direct way of obtaining the axial stiffness $E_1$ of the bolt is by measuring it in an uniaxial tensile test. In total 7 bolt specimens has been tested.

### 2.6.1 Method

The equipment used for this test was a uniaxial testing machine and two extensometers as shown in Figure 2.16 each specimen was placed in the testing machine and clamped in both ends. The extensometers were then placed on both sides such that they would measure the same section to ensure the quality of the measurement.

During testing the specimens were loaded to 60-70kN, based on an estimate. The clamping pressure was increased until no slippage was registered in the measurements, which would cause the specimens to crack due to transverse compression. This is not believed to have influenced the axial stiffness, since the fibers would remain intact.

Each specimen was loaded and unloaded twice during a test, where the first load cycle allowed the specimen to settle into place and ensure that only elastic strain was measured in the second load cycle.

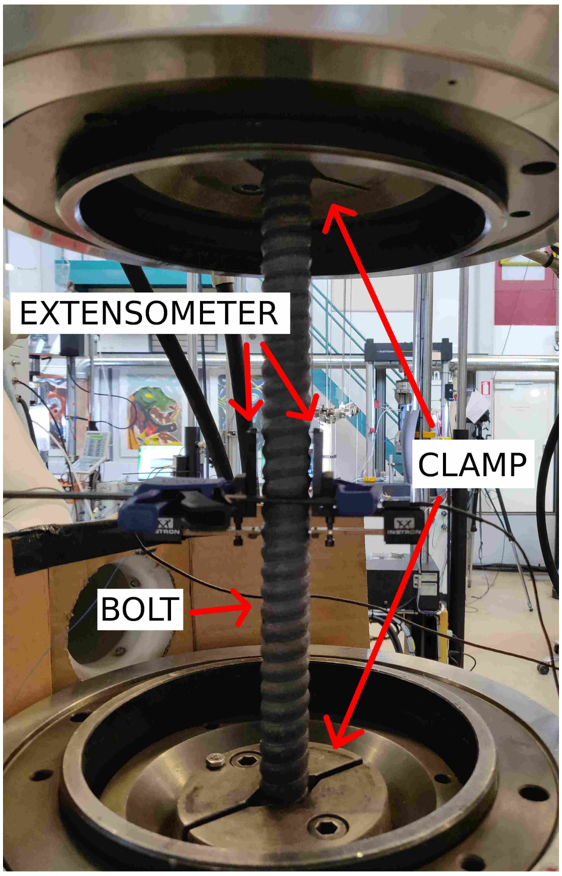

Figure 2.16: Test setup for the tensile test

### 2.6.2 Data and Data treatment

The load-strain curves in Figure 2.17 are obtained from the experiment and are all linear, which indicates pure elastic strain. The axial stiffness $E_{1bolt}$ is found from Eq. 2.24 as the stress-strain relationship, using the average cross sectional area $A_{bolt}$, from Table 2.7.

$$E = \frac{FA}{\epsilon} \tag{2.24}$$

The obtained axial stiffness $E_{\text{1bolt}}$ for each specimen is shown in Table 2.11. The fiber stiffness $E_{\text{f}}$ can then be isolated from Eq. 2.25, using the fiber volume fraction $V_{\text{fbolt}}$ from Table 2.8 and the matrix stiffness $E_{\text{m}}$ from the literature in Table 2.1.

$$E_{1bolt} = V_{\text{fbolt}} E_{\text{f}} + (1 - V_{\text{fbolt}}) E_{\text{m}} \tag{2.25}$$

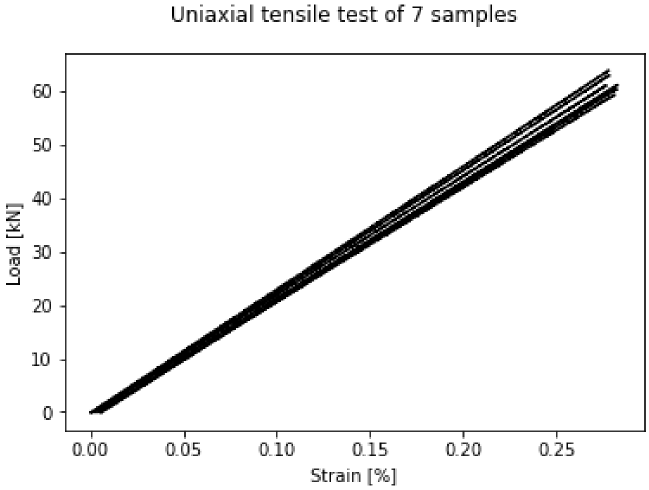

Figure 2.17: Setup of the tensile test

### 2.6.3 Results

The measured stiffness values from the tensile tests are reported in Table 2.11.

Table 2.11: Obtained axial stiffness $E_{1bolt}$ for the GFRP bolt in uniaxial tension, with $A = 442$mm

| Specimen | $E_{1bolt}$ [GPa] |
|---|---|
| 1 | 51.97 |
| 2 | 48.29 |
| 3 | 51.26 |
| 4 | 49.17 |
| 5 | 50.00 |
| 6 | 49.94 |
| 7 | 49.14 |
| *mean* | 49.97 |
| *sd* | 1.28 |

The mean value for $E_{1bolt}$ has been used to calculate the fiber stiffness in Table 2.12, based on Eq 2.25.

Table 2.12

| *specimen* | $E_{bolt}$ [GPa] | $E_{matrix}$ [GPa] | $E_{fiber}$ [GPa] |
|---|---|---|---|
| *RoBo*_01 | 49.97 | 3.4 | 72.08 |
| *RoBo*_02 | 49.97 | 3.4 | 72.71 |
| *RoBo*_03 | 49.97 | 3.4 | 72.62 |
| *RoBo*_04 | 49.97 | 3.4 | 72.01 |
| *mean* | | | 72.35 |

### 2.6.4 Discussion

The obtained fiber stiffness in Table 2.12 are exactly the same as the stiffness found in literature in Table 2.1, which indicates good quality results from microscopy and tensile testing. This method can also be used to determine the average fiber volume fraction $V_{\mathrm{f,bolt}}$ if the fiber stiffness is known.

## 2.7 Discussion and conclusion

This chapter has covered the necessary theory to describe the glass fiber bolt as a transverse isotropic material. It was found that all elastic parameters could be calculated based on two elastic parameters for each component along with the fiber volume fraction of the composite.

Four different experiments have been carried out to determine those parameters, where a good agreement was found between the obtained results. The matrix burn-off method and uniaxial tensile test requires little analysis, but the results are average values for the whole samples, which might not properly describe the material. The microscopy on the other hand allows for advanced analysis of the cross sectional pattern to detect inconsistencies in the material. Such as, with the rock bolt, where different fiber volume fractions were found for the core and thread. However, for this project it is assumed that the average values over the whole cross area are sufficient to describe the elastic parameters of the rock bolt.

The calculated parameters from this chapter are shown in Table 2.13

$E_2$, $G_{12}$, $G_{23}$ and $v_{23}$ are either directly or indirectly based on the semi-empirical equation from Halpin and Tsai (1967), with $\xi = 2$. There might be other values for $\xi$ that are more suitable for this GFRP bolt, but that will require experimental data on $E_2$ and $G_{12}$, which has not been covered in this project.

Table 2.13: Elastic parameters of the rock bolt

| Parameter | Value | unit | Method | ref | Notes |
|---|---|---|---|---|---|
| $V_f$ | 0.675 | [-] | Microscopy | Table 2.8 | |
| $E_f$ | 72.35 | [GPa] | Tensile test | Table 2.12 | |
| $v_f$ | 0.22 | [-] | Literatture | Table 2.1 | (Barbero, 2017) |
| $E_m$ | 3.4 | [GPa] | Literatture | Table 2.1 | (Barbero, 2017) |
| $v_m$ | 0.38 | [-] | Literatture | Table 2.1 | (Barbero, 2017) |
| $E_1$ | 49.97 | [GPa] | Tensile test | Table 2.11 | |
| $E_2$ | 17.98 | [GPa] | Halpin-Tsai | Eq. 2.4 | $\xi = 2$ |
| $G_{12}$ | 5.39 | [GPa] | Halpin-Tsai | Eq. 2.10 | $\xi = 2$ |
| $G_{23}$ | 6.41 | [GPa] | $\frac{1}{2}E_2/(1+v_{23})$ | Eq. 2.12 | |
| $v_{12}$ | 0.26 | [-] | $(1-V_f)v_\mathrm{m} + V_f v_\mathrm{f}$ | Eq. 2.6 | |
| $v_{23}$ | 0.40 | [-] | $1 - v_{21} - \frac{E_2}{3K}$ | Eq. 2.7 | |

# 3 Full Scale Laboratory Testing

## 3.1 Introduction

Full scale testing is the most direct way of evaluating the performance of rock bolt in a laboratory. This typically involves installing the rock bolts into concrete blocks to simulate conditions in rock. An illustration for a rock bolt in an opening fracture is shown in Figure 3.1.

Fully grouted rock bolts are typically installed into the rock mass, by first drilling a hole, then filling it with grout and finally pushing the bolt into the hole as shown in Figure 3.2.

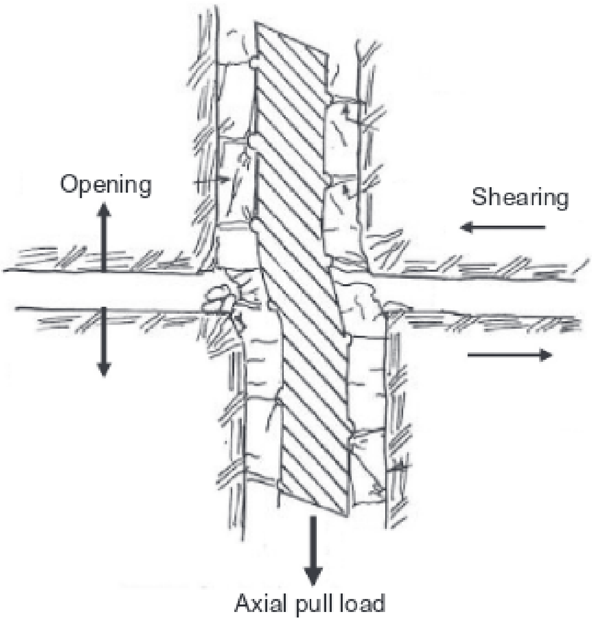

Figure 3.1: Illustration of a bolt in an opening fracture (Snyder, 1983)

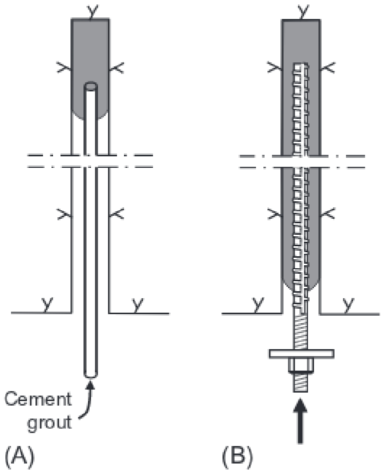

Figure 3.2: Installation procedure of a rock bolt (Li, 2017)

Previous testing has shown that steel rock bolts are able to maintain their load capacity in shear, because they are able to bend and crush the grout underneath them, effectively changing the angle relative to the joint and fail in tension (Li, 2017).

GFRP rock bolts are known to be much weaker in shear than in tension, but experiments performed by Gilbert et al. (2015) indicates that grout strength has a big influence on the shear strength of the tested GFRP bolts. Where the strength of the bolt was higher for the weaker grouts.

Table 3.1: Test log

| Test | Installed [dd-mm-yy] | Tested [dd-mm-yy] | Notes |
|---|---|---|---|
| 1 | 02-11-18 | 07-11-18 | Bolt rigg deformed during testing |
| 2 | 07-11-18 | 12-11-18 | |
| 3 | 14-11-18 | 21-11-18 | |
| 4 | 21-11-18 | 26-11-18 | |
| 5 | 11-01-19 | 14-01-19 | |
| 6 | 17-01-19 | 21-01-19 | |
| 7 | 21-01-19 | 24-01-19 | |
| 8 | 27-01-19 | 31-01-19 | |

### 3.1.1 Test Setup

The reported tests in this chapter has been carried out on the NTNU bolt rig, illustrated in Figure 3.3.

The bolt rig is a steel frame, that holds two concrete cubes, each measuring 950 × 950 × 950 mm. The bolt is installed in a hole, that is drilled through both cubes. The frame restricts each cube to uniaxial displacement, with one dedicated to axial tension and the other to lateral shear. Three hydraulic jacks are used to apply load to the cubes, where two are dedicated to applying axial tension and one to lateral shear

The concrete block consists of high strength concrete with a compressive strength over 100MPa. The used grout is a cement water mixture referred to as "Byggcement CEM II/A-LL 42,5 R" with $w/c = 0.35$

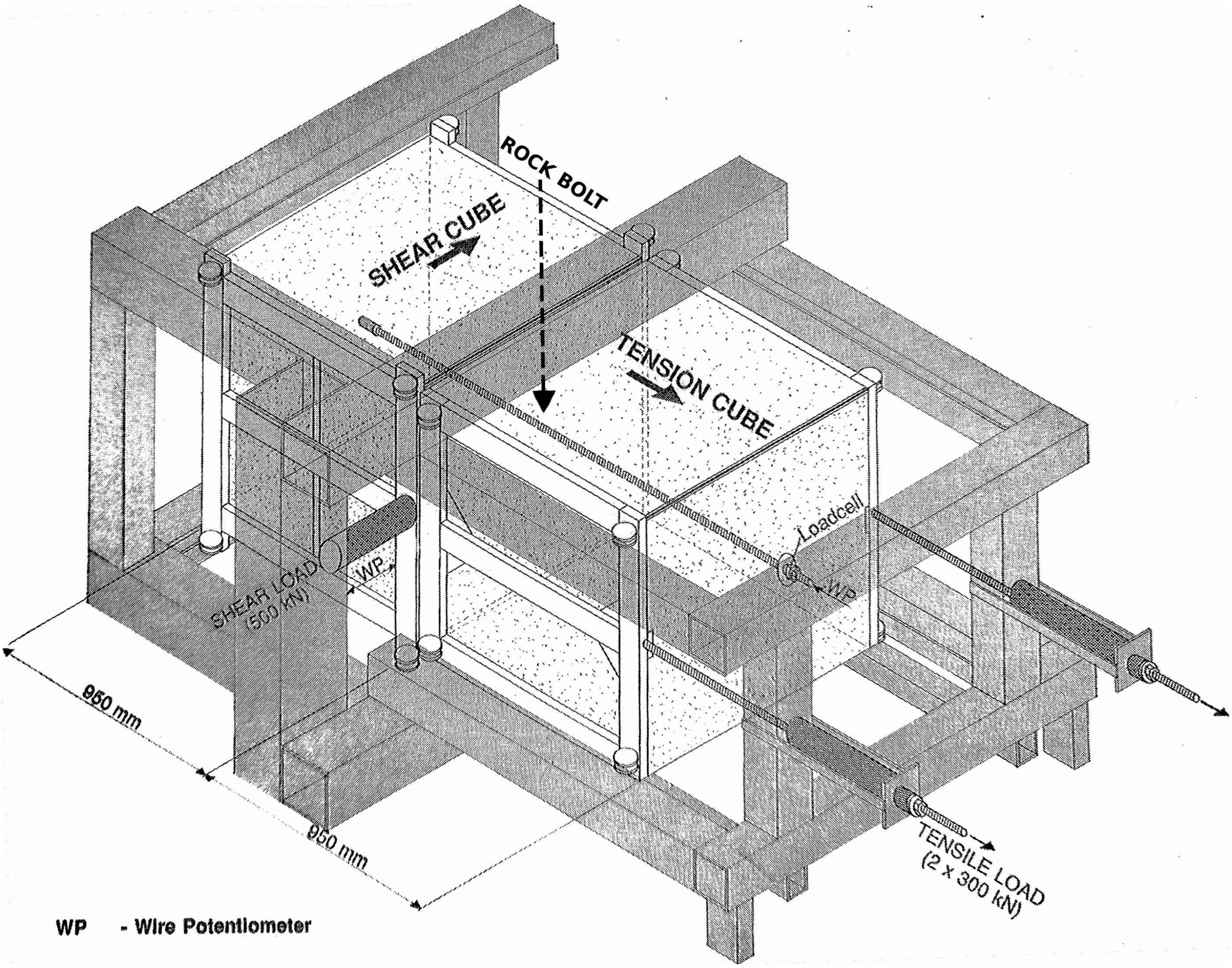

Figure 3.3: Schematic illustration of the NTNU bolt rig (Stjern, 1995)

## 3.2 Method

### 3.2.1 Test Preperation

The concrete cubes are cast as solid cubes, which requires holes to be drilled, before a bolt can be installed. This was done using a hammer drill, which leaves a rough surface within the hole and allows for a good bond with the grout. Multiple tests can be carried out, using the same block pair, as long as the bolts are installed along the plane of the hydraulic jacks, to ensure the loads are transferred properly to the bolt.

The drilling procedure is illustrated in Figure 3.4, where the drilling is initiated in one block (Fig: 3.4 a). Chunks of concrete breaks off the cube when the drill breaks through, which causes an uneven surface (b). The block is flipped, before the drilling continues through the next block (c), which results in a hole through both blocks with a smooth gap between them. The finished holes were then rinsed with water, to remove any loose particles left from the drilling.

A rubber seal is installed between the concrete blocks and the hole is plugged in one end prior to the grouting, to prevent the grout from leaking. This would result in a 6mm gap between the blocks. The grout used in this experiment is a mix of cement and water, which was mixed to a consistent mass, using a hand held mixer. The grout was pumped into the hole as shown in Figure 3.5 (a) not filling the hole completely to leave space for the bolt (Fig 3.5 b) The bolt is pushed in to the hole (Fig 3.5 c) displacing the excessive grout and leaving the bolt fully encapsulated in grout (Fig 3.5 d).

Two wire potentiometers were used to measure the displacement of the cubes, during the tests. One was attached to the tension cube right above the bolt and the other attached to the shear cube under the load applying jack as shown in Figure 3.3 A load cell was attached to the end of the bolt between the nut and face plate. In order to measure if any load was applied to the face plate under testing, which would indicate a poor grout quality.

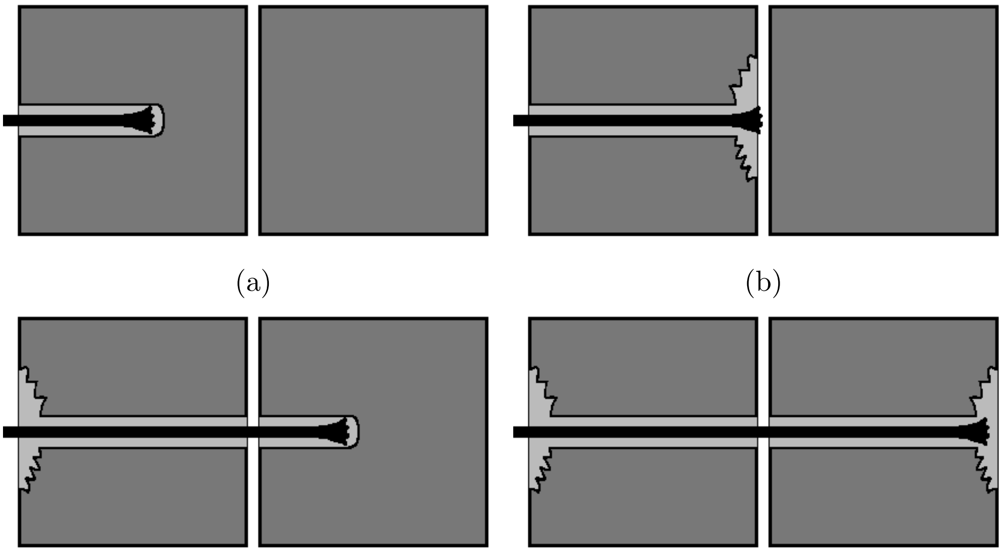

(a) (b)

(c) (d)

Figure 3.4: Procedure of drilling through the concrete blocks

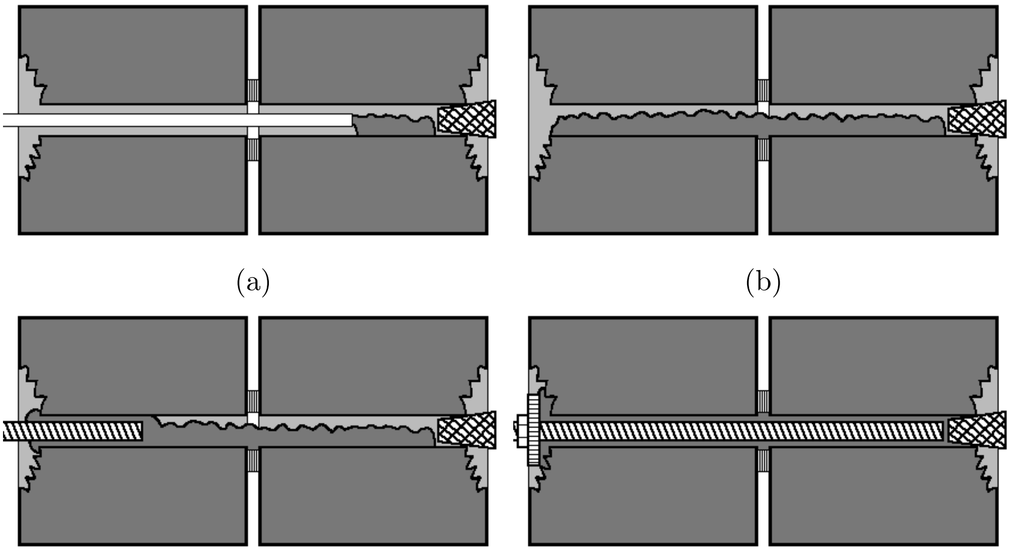

(a) (b)

(c) (d)

Figure 3.5: Procedure of installing a bolt

### 3.2.2 Test Procedure

The load applied to each cube with the hydraulic jacks, was controlled by manually adjusting valves on the hydraulic circuits. For a pure tensile test, only a tensile load was applied, while for the shear test only shear load was applied. When testing performance under combined loading, load was applied to both cubes, while tracking the displacement measured with the wire potentiometers in real time. A specific displacement angle could be achieved by adjusting the load on each cube, such that the ratio between the displacement of the cubes would give the desired angle.

Prior to the initiation of a test, the system was loaded slightly and relieved again in order to remove slack in the system. All instruments were then zeroed and the system was loaded again until bolt failure.

During testing, the applied load and the displacements of the blocks are logged every 0.5 second.

In total, 8 bolts were tested on the bolt rig, following the described procedure with the test log shown in Table 3.1. The grout curing time was minimum 3 days.

# 3.3 Data and Data Treatment

## 3.3.1 Loads and Displacements

The load and displacement applied to the individual cubes was logged throughout the test resulting in the plots shown in Figure 3.6, using test 4 and 8 as examples. The remaining plots are available in Appendix. The ultimate force $F$ and displacement $U$ for each test is summarized in Table 3.2, where the number denotes the cube and therefore the direction with $U_1, F_1$ being axial tension and $U_2, F_2$ lateral shear.

Table 3.2: Ultimate Load and Displacement

| Test | $U_1$ [mm] | $U_2$ [mm] | $F_1$ [kN] | $F_2$ [kN] |
|---|---|---|---|---|
| 1 | 11.8 | 0.0 | 444.1 | 0.0 |
| 2 | 16.2 | 0.0 | 448.4 | 0.0 |
| 3 | 12.0 | 12.9 | 378.2 | 73.0 |
| 4 | 10.0 | 9.9 | 419.0 | 49.0 |
| 5 | 0.0 | 20.1 | 0.0 | 158.6 |
| 6 | 1.4 | 21.8 | 111.5 | 119.6 |
| 7 | 6.8 | 20.8 | 173.6 | 97.5 |
| 8 | 5.9 | 21.2 | 175.8 | 124.7 |

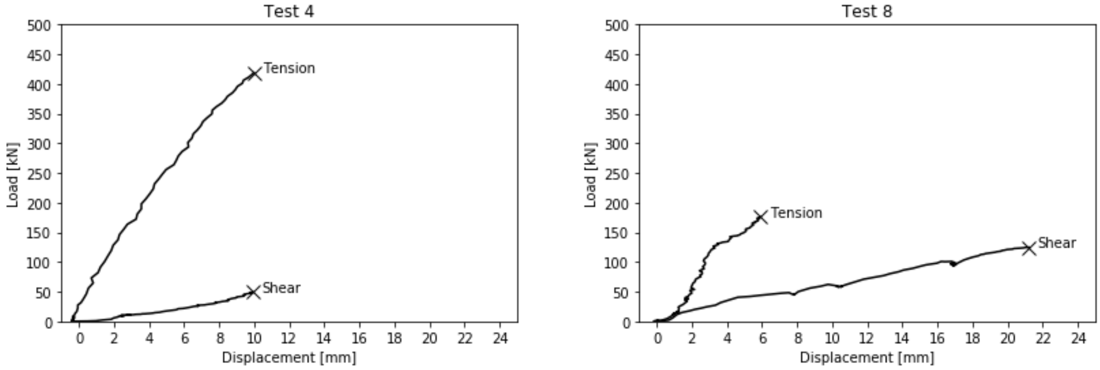

(a)

(b)

Figure 3.6: Load-Displacement curves

### 3.3.2 Load and Displacement Angle

The load angle $\alpha_F$ and displacement angle $\alpha_U$ are defined by Eq. 3.1 and 3.2.

$$\tan \alpha_F = \frac{F_2}{F_1} \tag{3.1}$$

$$\tan \alpha_U = \frac{U_2}{U_1} \tag{3.2}$$

The displacement angles were not kept constant during the tests, due to lack of control in the experiment. This can be seen from the relationship between the loads and between the displacements in Figure 3.7. The reported load and displacement angles from the tests are based on the ultimate loads and displacements.

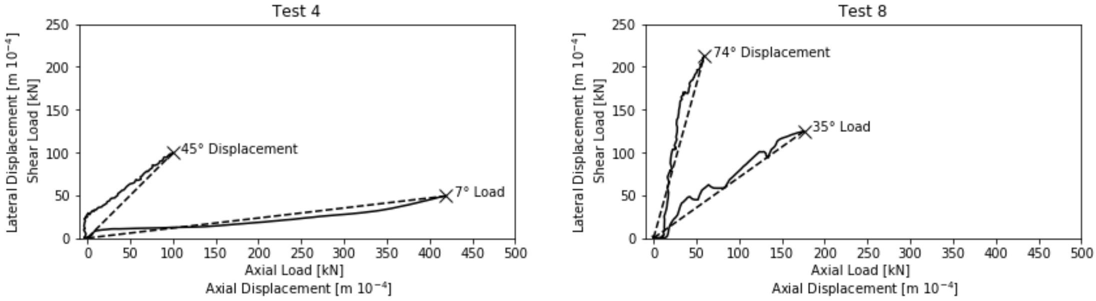

(a)

(b)

Figure 3.7: Relationship between tensile and shear load and axial and lateral displacement

### 3.3.3 Displacement Rate

The displacement rate was not kept constant, due to a lack of control in the experiment. Figure 3.8 shows the total displacement over time for test 4 and 8, with the remaining plots in Appendix. The reported displacement rate is selected in the region between 80% and 95% of the total displacement.

Another way to display the results, that better translate into shearing of a fracture, are in terms of total load $F_{total}$ and total displacement $U_{total}$, given by Eq. 3.3.

$$F_{total} = \sqrt{{F_1}^2 + {F_2}^2} \tag{3.3}$$

$$U_{total} = \sqrt{{U_1}^2 + {U_2}^2} \tag{3.4}$$

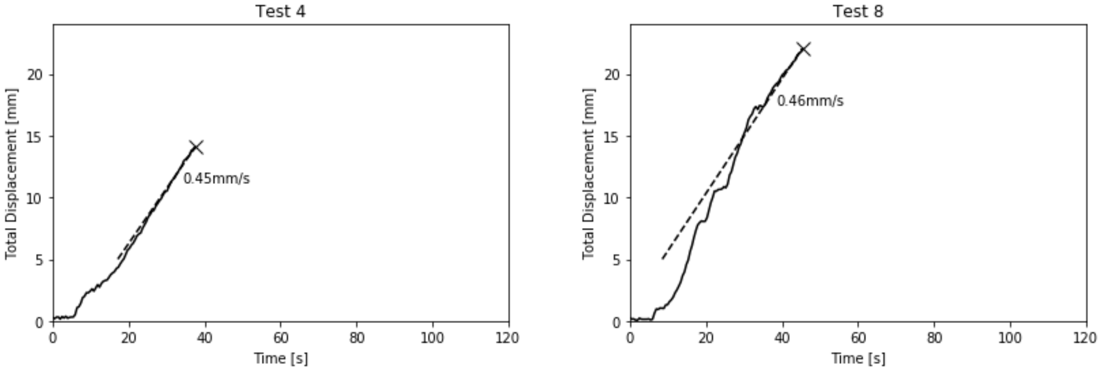

(a) (b)

Figure 3.8: Total displacement vs time

Where $C$ is a placeholder for the applied force $F$ or the displacement $U$. A load-displacement plot of all test, in terms of $F_{total}$ and $U_{total}$, is shown in Figure 3.9

## 3.4 Results

A summary of the results is shown in Table 3.3.

Table 3.3: Summary of Results

| Test | $U_{total}$ [mm] | $\alpha_U$ [°] | $F_{total}$ [kN] | $\alpha_F$ [°] | $V_{total}$ [mm/s] | $t_{curing}$ [days] |
|---|---|---|---|---|---|---|
| 1 | 11.8 | 0.0 | 444.1 | 0.0 | 0.32 | 5 |
| 2 | 16.2 | 0.0 | 448.4 | 0.0 | 0.42 | 5 |
| 3 | 17.6 | 47.1 | 385.1 | 10.9 | 0.38 | 7 |
| 4 | 14.1 | 44.8 | 421.9 | 6.7 | 0.45 | 5 |
| 5 | 20.1 | 90.0 | 158.6 | 90.0 | 0.18 | 3 |
| 6 | 21.9 | 86.4 | 163.5 | 47.0 | 1.01 | 4 |
| 7 | 21.9 | 72.0 | 197.5 | 29.3 | 0.37 | 3 |
| 8 | 22.0 | 74.4 | 215.5 | 35.4 | 0.46 | 4 |

### 3.4.1 Load-Displacement Curves

Load displacement curves are plotted for all tests in Figure 3.9, where the curves appear to be divided into two groups with different characteristics.

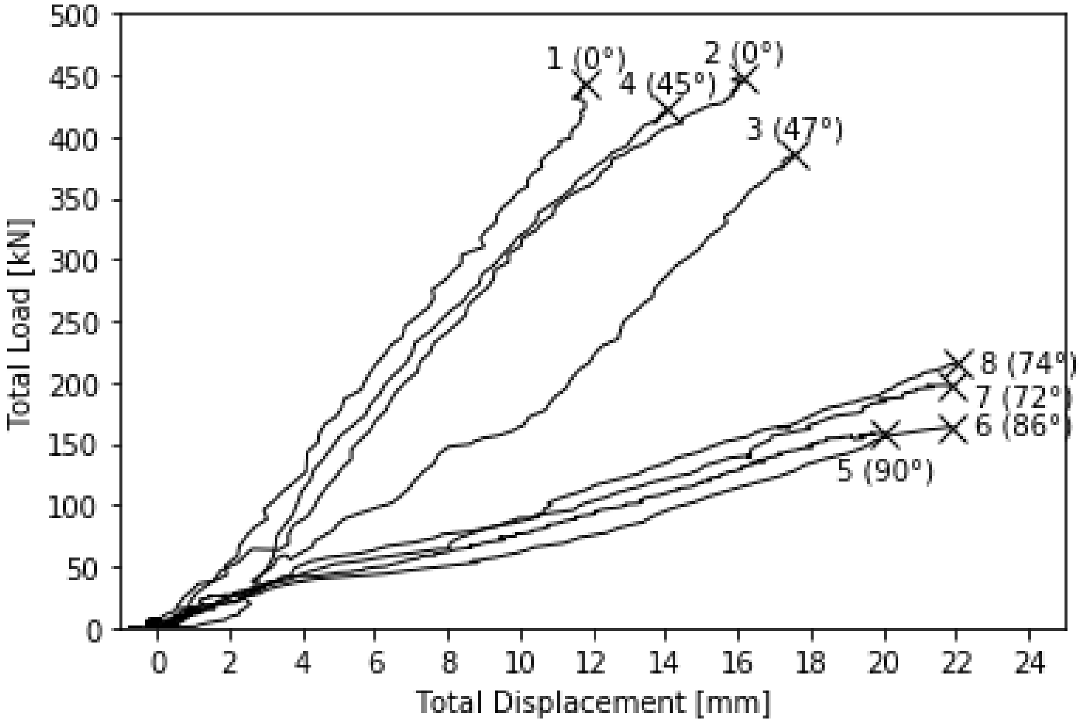

Figure 3.9

### 3.4.2 Failure Pattern

The failure patterns of the tested bolts are shown in Figure 3.10 and 3.11, Where some characteristics can be observed at different displacement angles.

- 0° (Fig 3.10a, 3.10b: The failure zone has many small bundles of fibers sticking out. The amount of visible threading indicates that the failure has initiated within the concrete cubes.
- 45° (Fig 3.10c, 3.10d): The failure appear similar to the ones at 0° however the threading appears to be more intact, where it is facing away from the relative shear direction. The amount of visible threading indicates that the failure has initiated within the concrete cubes.
- 70°-90° (Fig 3.11): The failure pattern is very different from the ones at 0°-45°, with little to no fibers sticking out and only a small amount of threading visible, indicating that the failure happened between the concrete cubes.

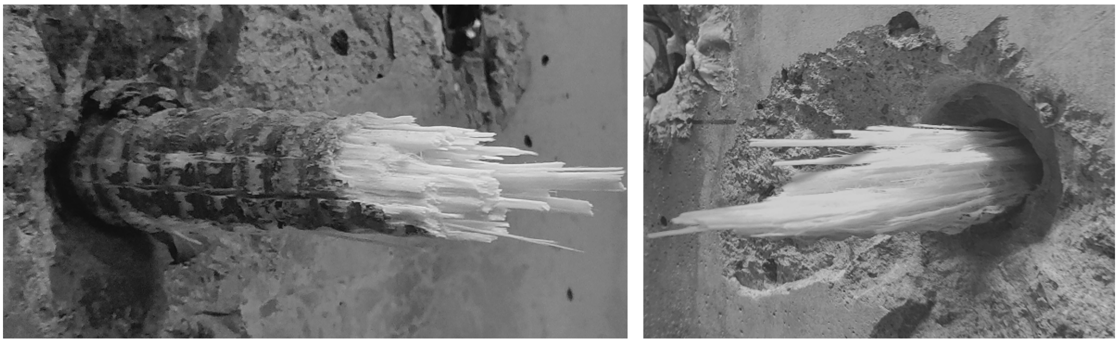

(a) Test no. 1, at 0° displacement angle

(b) Test no. 2, at 0° displacement angle

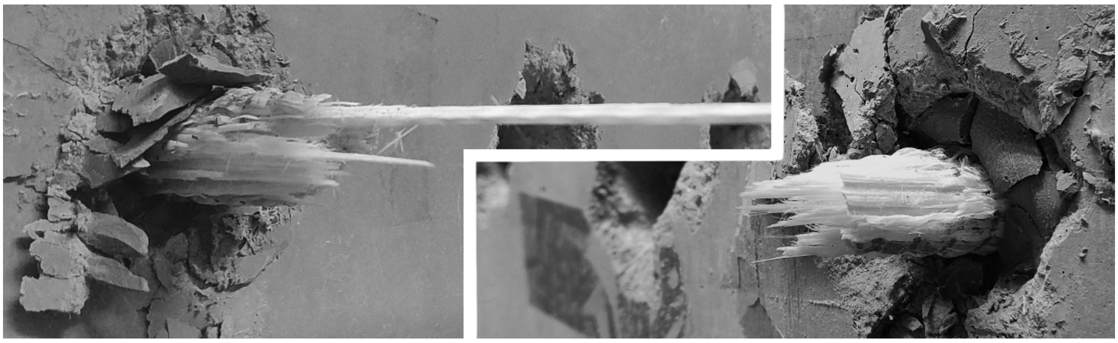

(c) Test no. 3, at 47° displacement angle

(d) Test no. 4 at 45° displacement angle

Figure 3.10: Post failure images of the rock bolts, taken in the shear direction, with the shear cube to the left and tension cube to the right

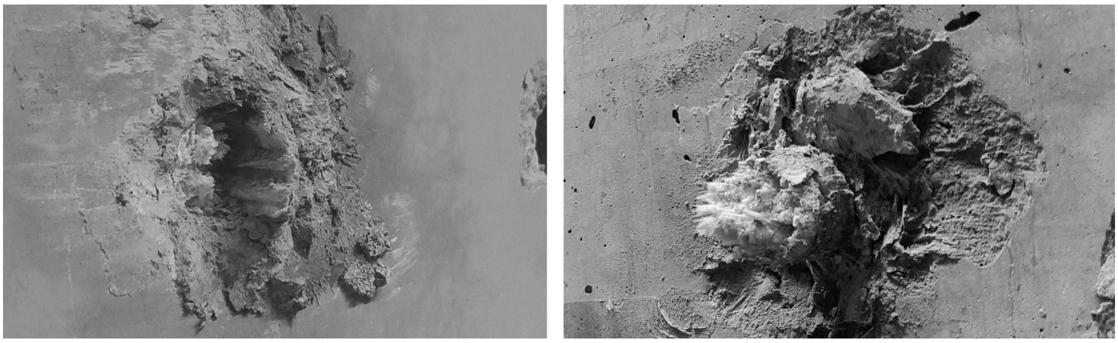

(a) Test no. 5, at 90° displacement angle

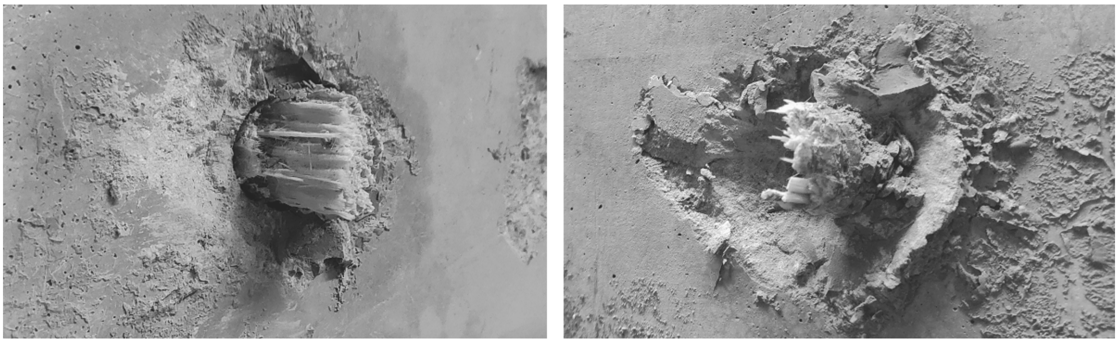

(b) Test no. 6, at 86° displacement angle

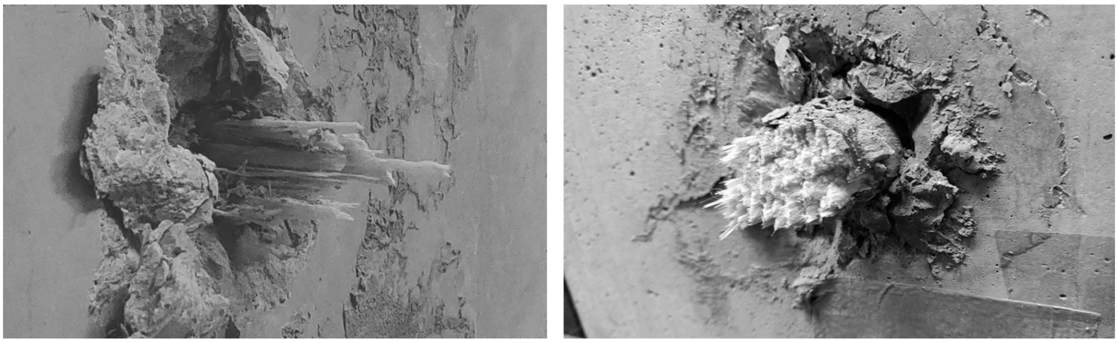

(c) Test no. 7, at 72° displacement angle

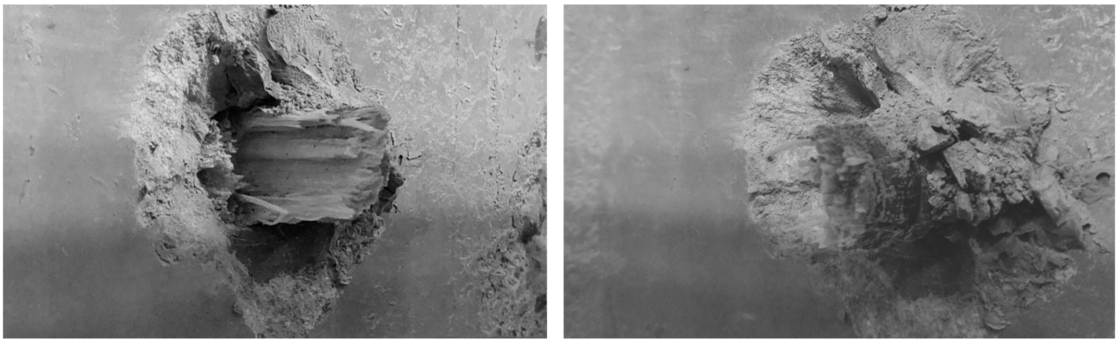

(d) Test no. 8 at 74° displacement angle

Figure 3.11: Post failure images of the rockbolts, taken in the shear direction, with the shear block to the left and tension cube to the right

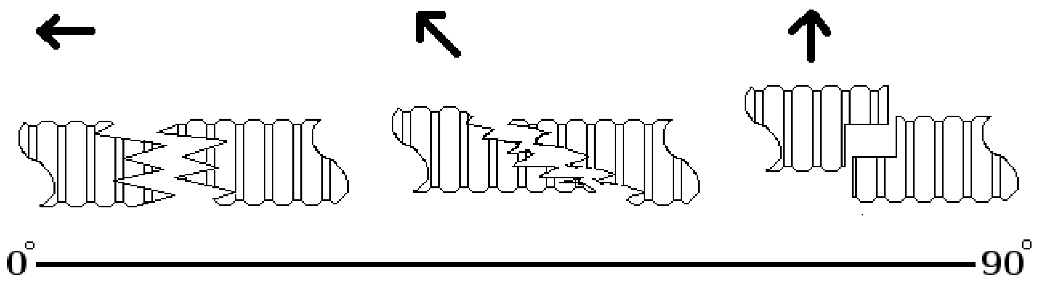

(a) Summary of failure patterns, observed in Figure 3.11 and 3.10

## 3.5 Discussion and Conclusion

The results from Table 3.3 are visualized in Figure 3.13 as ultimate total load and displacement plotted in relation to the load and displacement angle. It is evident that there is no obvious relation between the ultimate total load and displacement angle for the whole range from 0 to 90°. The bolt appears to maintain its strength for up to 47° displacement, from where there is a relative steep drop to the failure load at 72° displacement, followed by a less steep drop to 90°. A similar grouping of the results can be seen in Figure 3.13b, where the ultimate total displacement increase with the displacement angle, while having a steeper increase between 47° and 72°.

The observations on failure patterns, from Figure 3.11 and 3.10, has been summarized in Figure 3.12a where it is shown that in pure tension, the failure surface of the bolt appear like a brush, with fibers pulled out between each other. At 45° there are less fibers sticking out and the point of failure seem to be in a zone, where the bolt is likely to experience the highest amount of tensile stress, due to bending of the bolt. The failure pattern then dramatically changes for failures with a displacement angle higher than 72°, where there are almost no fibers sticking out and in general appear much cleaner. The most notable difference is that the point of failure has shifted to the opposite side, which is a sign of a change in the failure mechanism, which will also explain the observed drops in strength.

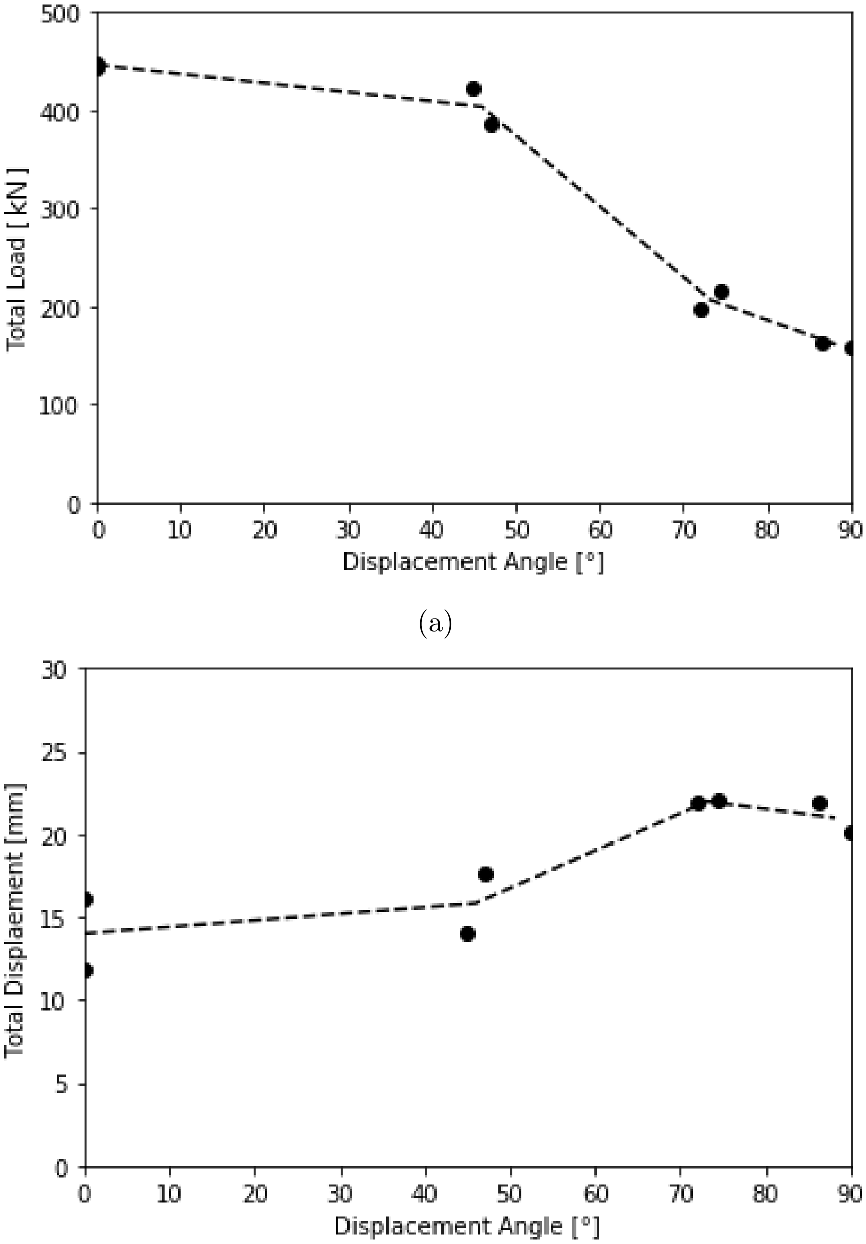

(a)

(b)

Figure 3.13: ultimate total load and total displacement plotted in relation to the displacement angle

# 4 Numerical Modelling

## 4.1 Introduction

The results obtained from the full scale test in chapter 3 were found for the whole system, which includes the rock bolt, the grout and the concrete cubes. The properties of the other materials will affect the performance of the rock bolt, especially the grout and the hole diameter, will influence the shear performance, since the grout has been crushed by the bolt while shearing.

A way to decompose the system and investigate the stresses in the bolt is through numerical modelling, which is carried out in this chapter with the Finite Element Method (FEM), using ABAQUS.

The procedure of this chapter is to establish a model with meaningful material parameters and to replicate the full scale test. The main problem with replicating the experiment is to define proper grout parameters. This is attempted with a calibration step, where different grout models are evaluated in a pure tension and pure shear scenario from the full scale test.

The best model from the calibration step is then used to run the test at different angles and observe the stresses and displacements experienced by the bolt.

The bolt is modelled with thread, which gives a rather complex surface contact between the bolt and grout at large deformations. It is therefore suggested by Abaqus Analysis User's Manual (2010) to be modeled using Explicit dynamic analysis.

### 4.1.1 Explicit Dynamic Analysis

Explicit dynamic analysis is available under Abaqus/Explicit. The practical difference between explicit and implicit analysis from in ABAQUS/Standard, is that the explicit analysis requires many small inexpensive increments, where larger increments can be made with implicit analysis.

ABAQUS/Explicit is also modelling in real time, where the stable time increment limit can be estimated from Eq. 4.1.

$$\Delta t \approx \frac{L_{min}}{c_d} \tag{4.1}$$

Where $L_{min}$ relates to the smallest element size in the model and $c_d$ is the dialational wave speed, given by Eq. 4.2.

$$c_d = \sqrt{\frac{\hat{\lambda} + 2\hat{\mu}}{\rho}} \tag{4.2}$$

With $\hat{\lambda}$ and $\hat{\mu}$ being effective Lamé's constants and $\rho$ the material density.

By assuming a constant $\Delta t$ the total number of increments required for the model is given by Eq. 4.3.

$$n = \frac{T}{\Delta t} \tag{4.3}$$

Where $T$ is the time period of the event being simulated.

Modelling in real time can be wasteful for quasi-static scenarios, which typically can take a long time. The computation time of a model can be reduced by either reducing the time period $T$ (time scaling) or increasing the material density $\rho$ (mass scaling). This can influence the results and therefore the energies in the model should be monitored, where the ratio of kinetic energy to internal energy should not be larger than 10%

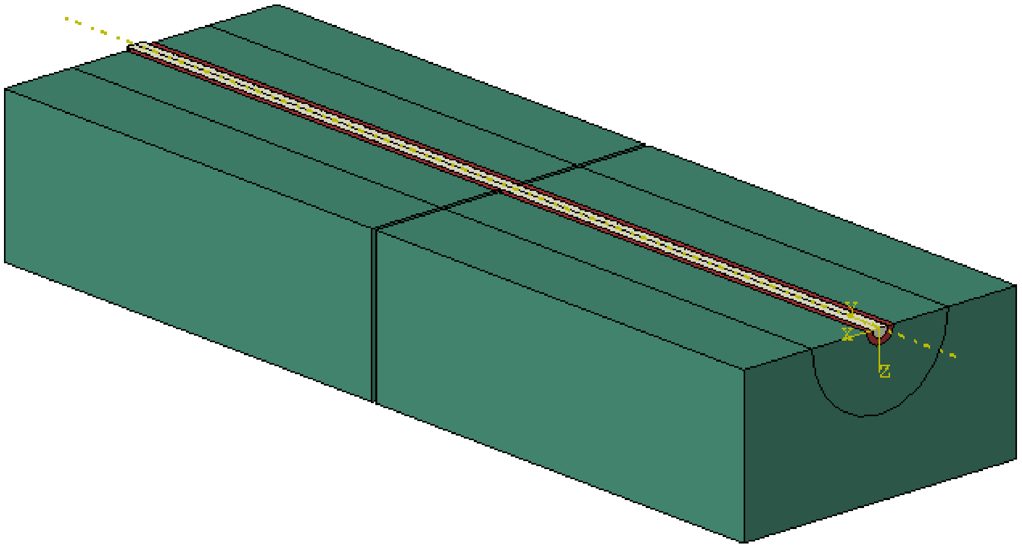

Figure 4.1: Full view of the geometry of the model

## 4.2 FEM Model

The model, in Figure 4.1, is created to replicate the NTNU bolt rig, described in Chapter 3. It consists of five parts, 2 concrete cubes, 2 sections of grout, and the GFRP bolt. Symmetry is utilized to reduce the number of elements in the model. The model should be able to simulate axial tension and lateral shear displacements, which limits the model to one plane of symmetry.

### 4.2.1 Geometry

Each part of the model is created with the symmetry in mind and are therefore cut in half. Similar to the NTNU bolt rig, the bolt is placed through the two concrete cubes, with the grout as a connecting layer. An exploded view of the model can be seen in Figure 4.2 to better show off the different parts.

It should be noted that the bolt revolves around the y axis which causes tension to be applied in y and shear in the x direction.

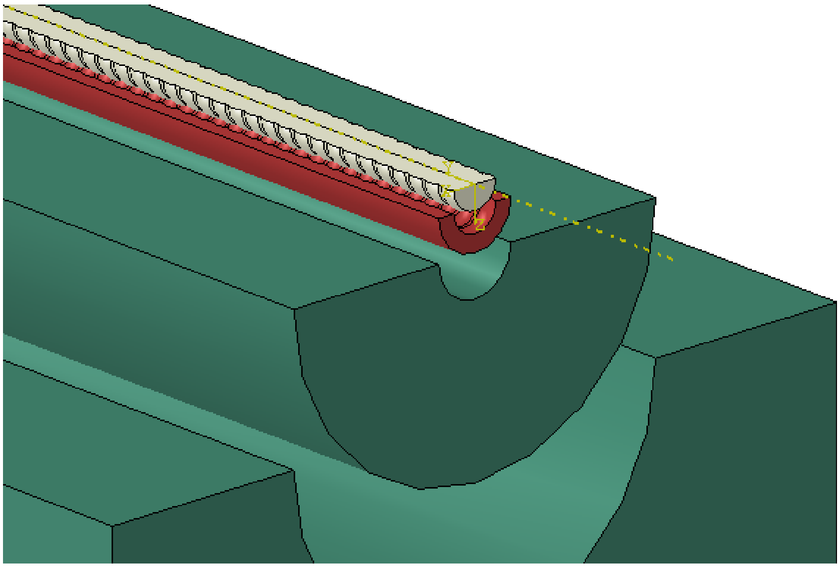

Figure 4.2: Exploded view of the tension cube

### Bolt

The bolt is designed as a bar with a core diameter of 23mm. For simplicity the thread is modelled axisymmetric as circular arches that revolves around the bar with a spacing of 2mm between them. The dimensions used to model the bolt are based on the measured dimensions in Table 4.1

Table 4.1: Dimensions of the GFRP bolt

| Outer Diameter | Pitch Diameter | Root width | Pitch |
|---|---|---|---|
| 25 mm | 24 mm | 2 mm | 10 mm |

### Grout

The grout is designed as a cylinder, where the outer surface, in contact with the inner concrete cube is smooth and the inner part is cut to fit the shape of the rock bolt. The outer grout diameter equal to the hole diameter, which is 40mm.

**Concrete cubes**

The concrete cubes are each split into two parts to simplify meshing. The inner part is a cylinder that connects the grout to the outer block. The outer block has a width of 400mm a 6mm gap was kept between the cubes as in the experiment

**Interfaces**

The bolt grout interface is modelled as a friction-less tangential interaction, Which causes the bolt to only interact with the grout through mechanical interlocking. The grout and blocks are stitched together, using tie constraints to form the tension and shear cube.

### 4.2.2 Boundary Conditions

The boundary conditions are similar to those of the NTNU bolt rig, where each cube is restricted to uniaxial displacement, with one dedicated to axial tension and the other to lateral shear. In the model the boundary conditions are applied to the outer part of the cubes on each side, parallel with the direction of displacement as shown in Figure 4.3. Displacements are applied to the outer cubes on the surface indicated with arrows.

### 4.2.3 Mesh

The mesh can be seen in Figure 4.3. A finer mesh was chosen for the bolt and grout, since those are the primary parts of interest. The smallest elements are approximately 1mm and the element size increases with the distance to the bolt.

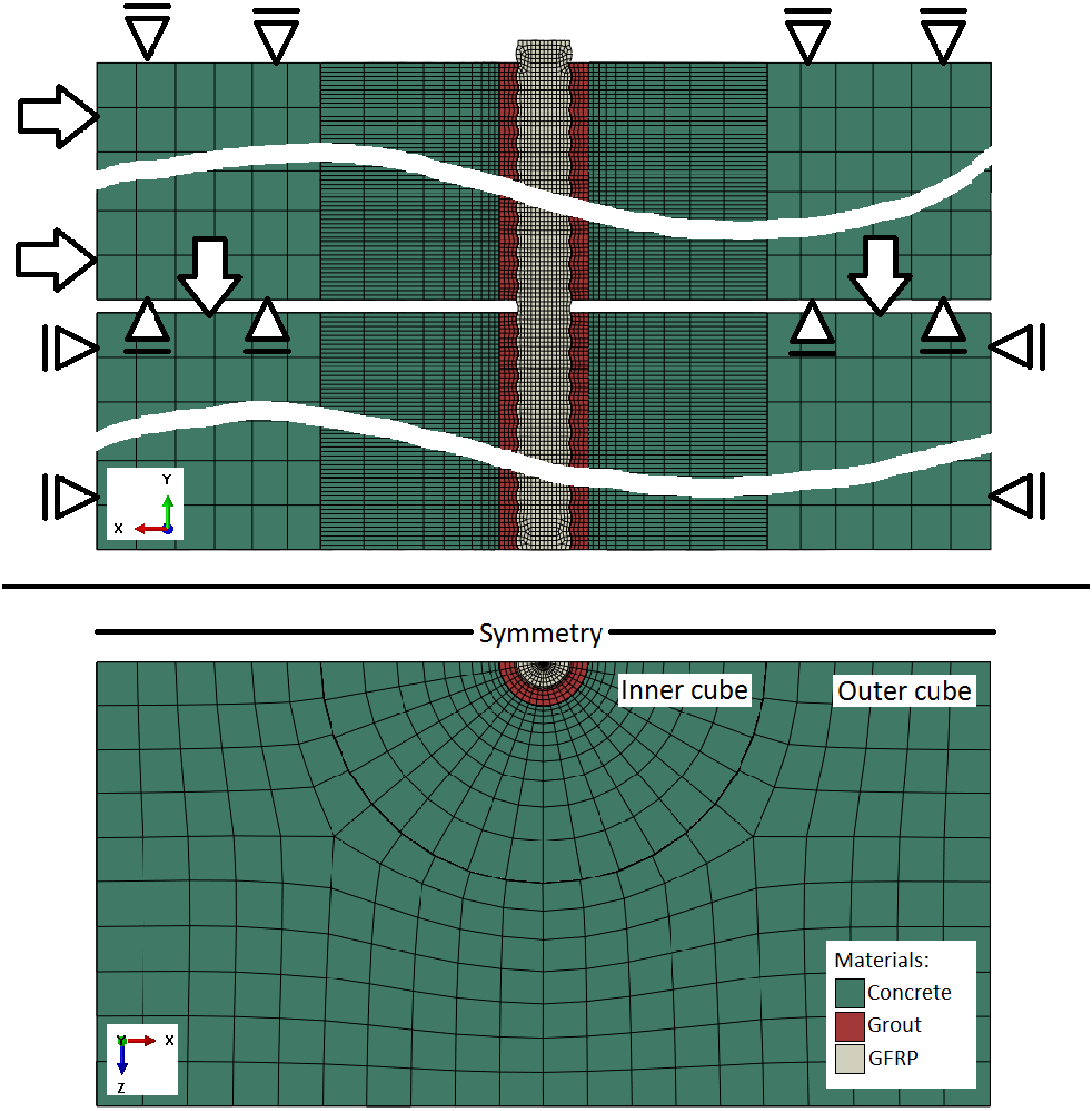

Figure 4.3: Overview of the model

## 4.3 Material Parameters

The material models and parameters determines the behaviour of the materials in the FE model. It is therefore important that they represent the material as accurate as possible.

### 4.3.1 GFRP

The GFRP material is described as an elastic transverse isotropic material, which has been described in Chapter 2. The used elastic parameters in Table 4.2 are taken from Table 3.3 and the density from the matrix burn-off method in Table 2.10

Table 4.2: Elastic Parameters for modelling GFRP

| $\rho$ [kg/m$^3$] | $E_1$ [GPa] | $E_2$ [GPa] | $G_{12}$ [GPa] | $G_{23}$ [GPa] | $v_{12}$ [-] | $v_{23}$ [-] |
|---|---|---|---|---|---|---|
| 2121 | 49.97 | 17.98 | 5.39 | 6.41 | 0.26 | 0.40 |

### 4.3.2 Concrete

The concrete is modelled as an isotropic material. No experiments has been carried out to estimate the elastic parameters of the concrete. The used parameters are shown in Table 4.3

Table 4.3: Elastic parameters for grout and concrete

| | $\rho$ [kg/m$^3$] | $E$ [GPa] | $v$ [-] |
|---|---|---|---|
| Concrete | 2400 | 45 | 0.2 |
| Grout | 2400 | 20 | 0.22 |

### 4.3.3 Grout

The grout is assumed to behave much like intact rock, which can be described as an elastic-brittle material Li (2017). where the used elastic parameters are given in Table 4.3

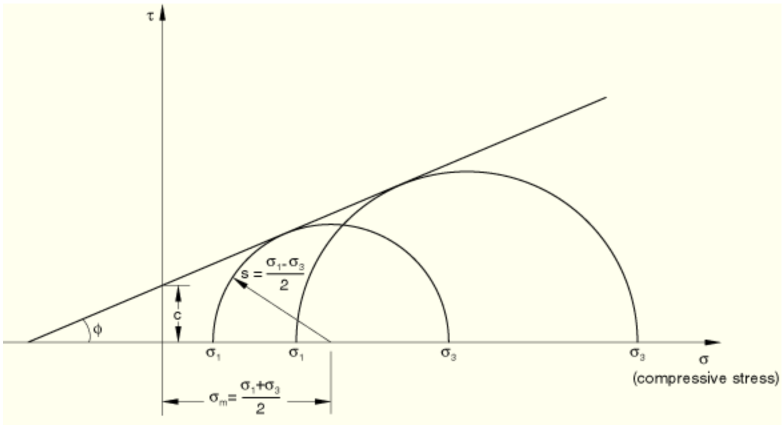

Figure 4.4: Mohr-Coulomb failure line fitted on Mohr circles (Abaqus Analysis User's Manual, 2010)

A strength of the grout is needed to define brittle failure and due to limited testing of the used grout, only information about the uniaxial compressive strength is available, which is based on previous testing, reported by Li et al. (2016). The two yield criteria considered for the grout is the Mohr-Coulomb and the Extended Drucker-Prager criterion. Both are defined in a similar manner, with the latter allowing for more extensions to be added in ABAQUS (Abaqus Analysis User's Manual, 2010). The selection of grout parameters is done through a calibration step, discussed in section 4.4.

### Mohr-Coulomb

The Mohr-Coulomb (MC) yield criterion is often used to describe the behavior of intact rock. (Li, 2017) From Abaqus Analysis User's Manual (2010), it is stated that the MC failure line is based on a best fit of several Mohr Circles, defined by the maximum and minimum principal stresses at failure of a material as seen in Figure 4.4. In practice this causes the material to behave stronger with increased confining pressure. The slope of the line is the material friction angle $\phi$ and the shear strength $\tau$ at $\sigma = 0$ is the cohesion $c$.

The cohesion $c$ can be calculated based on $\phi$ and an uniaxial compressive strength $UCS$ with Eq. 4.4.

$$c = \frac{UCS(1 - \sin\phi)}{2\cos\phi} \tag{4.4}$$

### Extended Drucker-prager

The Extended Drucker Prager (EDP) yield criterion is provided by ABAQUS. It can be used to approximate the MC criterion, while supporting further extensions, such as element removal. The EDP yield criterion requires three values, which are the DP friction angle $\beta$, the flow stress ratio $K$, and an uniaxial compressive strength $\sigma_{0c}$

A guide is provided by Abaqus Analysis User's Manual (2010) to convert MC parameters to EDP parameters, From the equations provided in equation 4.5 and 4.6

$$\tan\beta = \frac{6\sin\phi}{3-\sin\phi} \tag{4.5}$$

$$K = \frac{3-\sin\phi}{3+\sin\phi} \tag{4.6}$$

The effect of $K$ is an improved fit to the MC yield surface, as shown in Figure 4.5. $K = 1$ will cause the EDP surface to take shape as a circle and give a poor fit to the MC yield surface. The minimum value $K$ can take is 0.778, which corresponds to a MC friction angle $\phi = 22°$. If MC parameters with $\phi > 22°$ are converted it is suggested to use $\phi$ to calculate $\beta$, and have $K = 788$.

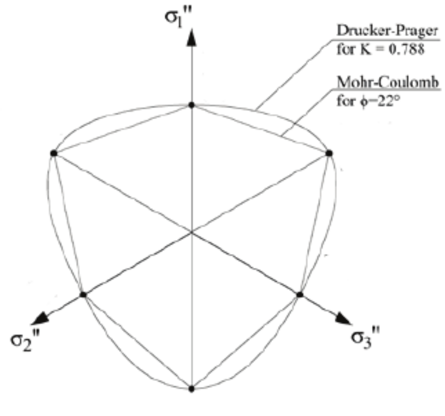

Figure 4.5: Mohr-Coulomb and Extended Drucker-Prager models match in the diviatoric plane for triaxial conditions, after (Józefiak et al., 2015)

## 4.4 Calibration of Grout

An attempt to calibrate the grout has been made, in order to find the most suitable parameters for either Mohr-Coulomb or Drucker-Prager.

### 4.4.1 Grout Parameters

From Li et al. (2016) it is provided that $UCS = 45\text{MPa}$ for the grout used in the full scale test in Chapter 3. With the defined UCS $c$ is calculated for $\phi = 15°, 17°, 20°, 22°, 25°$ with Eq. 4.4 to establish the MC parameters.

With the MC parameters established, $\beta$ and $K$ can then be calculated from Eq. 4.5 and 4.6. The found parameters are shown in Table 4.4. The materials are modelled as elastic-brittle by letting the values of $c$ and $\sigma_{0c}$ drop to 50% at 1% plastic strain.

Table 4.4: Parameters for Mohr-Coulomb and Drucker-Prager yield criteria

| $\phi$ [°] | $c$ [MPa] | $K$ [-] | $\beta$ [°] | $\sigma_{0c}$ [MPa] |
|---|---|---|---|---|
| 15 | 17.3 | 0.841 | 29.53 | 45 |
| 17 | 16.6 | 0.822 | 32.94 | 45 |
| 20 | 15.8 | 0.795 | 37.67 | 45 |
| 22 | 15.2 | 0.788 | 40.57 | 45 |
| 25 | 14.3 | 0.788 | 44.53 | 45 |

### 4.4.2 Method

The model has been run in a tension and shear scenario that follows test no. 2 and 5 from the full scale test in Chapter 3. The used loads and displacements are shown in Table 4.5. For the shear scenario the displacement $U_2$ was applied to the shear cube and the load was measured in the reactions on the tension cube. In the tension scenario, the displacement $U_1$ was applied to the tension cube and the loads were measured on the shear cube.

The model time was set to 1 second, and no mass scaling was applied.

Table 4.5: Loads and Displacements used for grout calibration

| Test | $U_1$ [mm] | $U_2$ [mm] | $F_1$ [kN] | $F_2$ [kN] |
|---|---|---|---|---|
| 2 | 16.2 | 0.0 | 448.4 | 0.0 |
| 5 | 0.0 | 20.1 | 0.0 | 158.6 |

### 4.4.3 Results

The results of the calibration step are shown in Figure 4.6. It can be seen that none of the material models are able to describe the grout behaviour and reproduce the experiment.

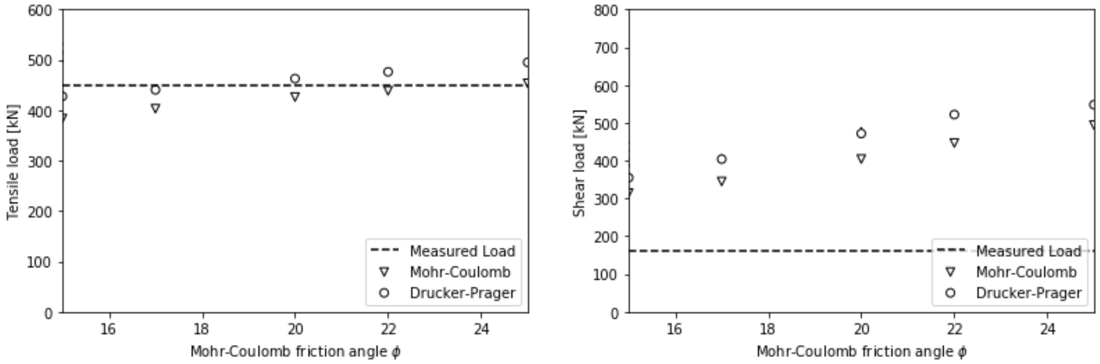

(a) calibration results in tension

(b) Calibration results in shear

Figure 4.6: Results of grout calibration, using Mohr-Coulomb and Drucker-Prager yeild criteria, in an elastic brittle scenario

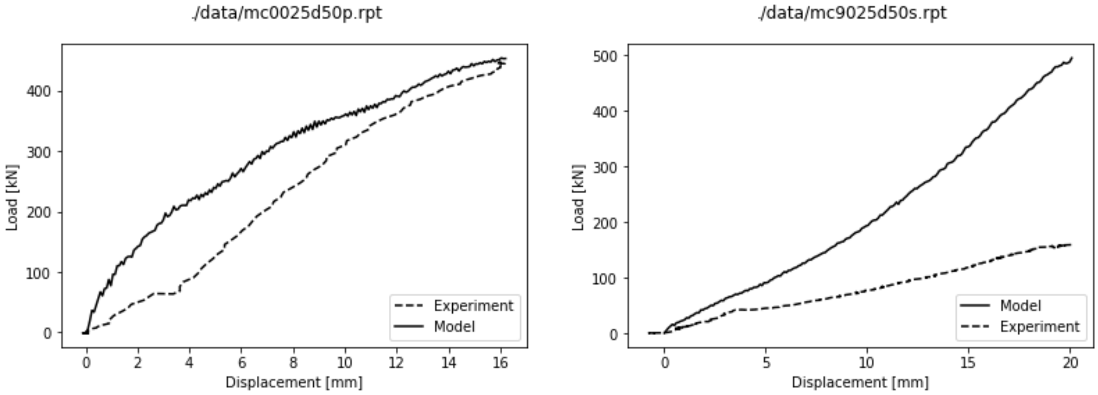

(a) MC model with $\phi = 25°$ in tension (b) MC model with $\phi = 25°$ in shear

Figure 4.7: Comparison of Load-Displacement curves

### Energy

The energy was monitored to ensure good quality of the model. The plots were very similar for all the calibration runs, so only one plot has been reported.

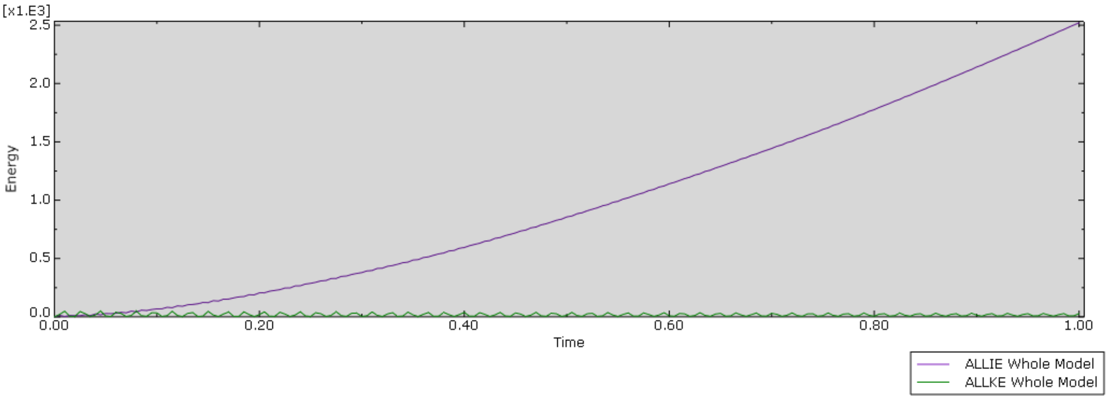

Figure 4.8: Plot of the internal energy (ALLIE) and the kinetic (ALLKE) for the whole model. Measured in the MC model with $\phi = 25°$ displacement in the shear scenario

### 4.4.4 Discussion

It was found that none of the investigated material models were able to reproduce the experiment in both tension and shear. The MC model with $\phi = 25°$ was able to give correct load in the tension scenario. Load-Displacement curves are shown in Figure 4.7, where it is shown that the curves from the model does not follow the curves from the full scale test. This could indicates that the used material model does not represent the grout very well.

A material model has to be selected to continue with the analysis and for that the elastic-brittle MC model with $\phi = 25°$ is selected, based on the match in tension. The maximum axial stress experienced by the bolt was found to be $\sigma_{22} = 1.2\text{GPa}$, which will be used to establish a failure criteria in the following section.

The kinetic and internal energy is compared, in Figure 4.8, where it is shown that the kinetic energy is well below the internal energy for most of the test. There are spikes observed in the beginning, where the kinetic energy is higher than the internal energy. This may lead to some inaccuracy in the model, but increasing the model time did not seem to have an effect on the results, so the model time was kept at 1 second.

## 4.5 Combined Displacement

A material model for the grout was established and can now be used to simulate displacement angles from 0 to 90 degrees at intervals of 10 degrees. To get a better understanding of how the stresses are distributed in the bolt in different loading conditions. A simple failure criteria is applied to see if it can indicate a trend between the ultimate load and displacement angle of ultimate load and load angle.

The applied failure criteria is based on a maximum stress criteria from Barbero (2017) where failure is assumed when either the ultimate axial stress $\sigma_{22\mathrm{u}}$ or the ultimate shear stress is reached $\tau_{12\mathrm{u}}$

$$\begin{aligned} \sigma_{22} &\geq \sigma_{22\mathrm{u}} \\ \|\tau_{12}\| &\geq \tau_{12\mathrm{u}} \end{aligned} \tag{4.7}$$

Where the strength parameters are

$$\sigma_{22\mathrm{u}} = 1200\mathrm{MPa} \tag{4.8}$$

and

$$\tau_{12\mathrm{u}} = \frac{F_2}{A_{bolt}} = \frac{159\mathrm{kN}}{442\mathrm{mm}^2} = 360\mathrm{MPa} \tag{4.9}$$

Where $F_2$ is the ultimate shear load from the full scale test in pure shear, taken from Table 3.2. And $A_{bolt}$ is the cross sectional area of the bolt, taken form Table 2.7.

### 4.5.1 Method

Displacements were applied to the model for each displacement angle in Table 4.6, where Lateral displacement was applied to the shear cube and Axial displacement to the tension cube. Each run was divided into 21 frames, in which the displacement and stresses were recorded along a line in the center and on the edge of the bolt, as shown in Figure 4.13, As for the grout calibration the model time was set to 1 second and no mass scaling was applied

### 4.5.2 Results

The reported results are selected from the frame where the failure criteria in Eq. 4.7 is met. It was found that displacement angles 0° to 70° failed in tension, while 80° and 90° failed in shear.

Table 4.6: Applied displacements

| Angle | Axial [m] | Lateral [m] |
|---|---|---|
| 00 | -0.0200 | 0.0000 |
| 10 | -0.0200 | -0.0035 |
| 20 | -0.0200 | -0.0073 |
| 30 | -0.0200 | -0.0115 |
| 40 | -0.0100 | -0.0084 |
| 50 | -0.0080 | -0.0095 |
| 60 | -0.0055 | -0.0095 |
| 70 | -0.0040 | -0.0110 |
| 80 | -0.0020 | -0.0113 |
| 90 | 0.0000 | 0.0100 |

### Stresses at 50° displacement

Images of stresses are just shown for 50°, since it is shows the same patterns at other displacement angles, with the exception of pure tension, which can be seen in Appendix along with the plot for pure shear.

Figure 4.9 shows the axial stresses in a combined loading condition at 50° Displacement angle, where both tension and compression can be seen along the edge of the bolt.

The transverse stresses at 50° displacement are shown in Figure 4.10. The transverse compression zone is located in the same areas of the bolt as the axial compression zones

The shear stresses at 50° displacement angle are displayed in Figure 4.11. where it is evident that the shear stresses are highest in the middle of the bolt.

The plastic strain of the yielded elements is shown in Figure 4.12, which shows large plastic strain where grout is pushed out by the deforming bolt.

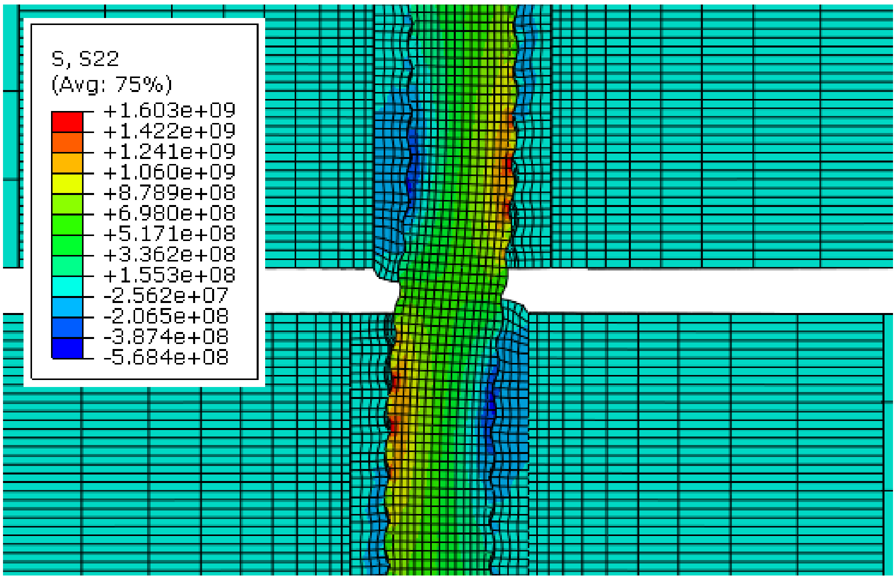

Figure 4.9: Axial stress at 50 degree displacement

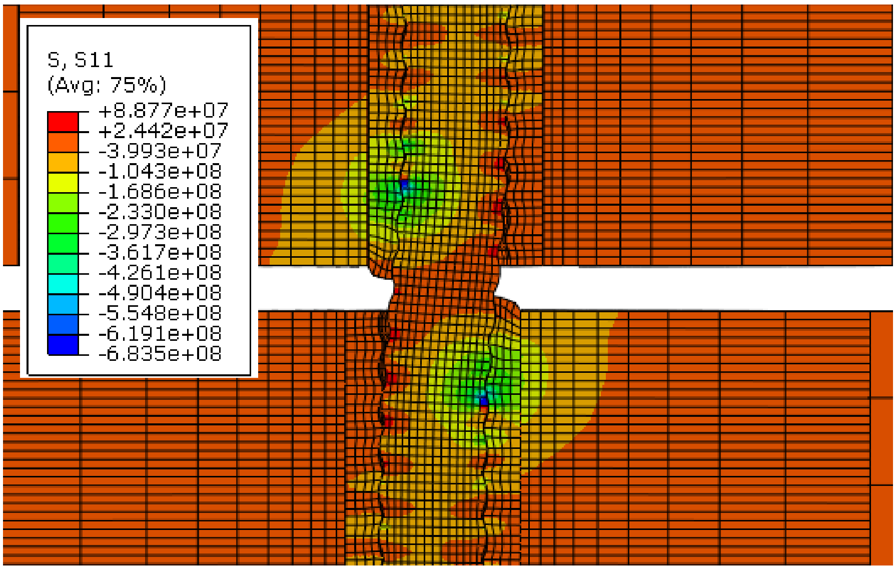

Figure 4.10: Transverse stress at 50 degree displacement

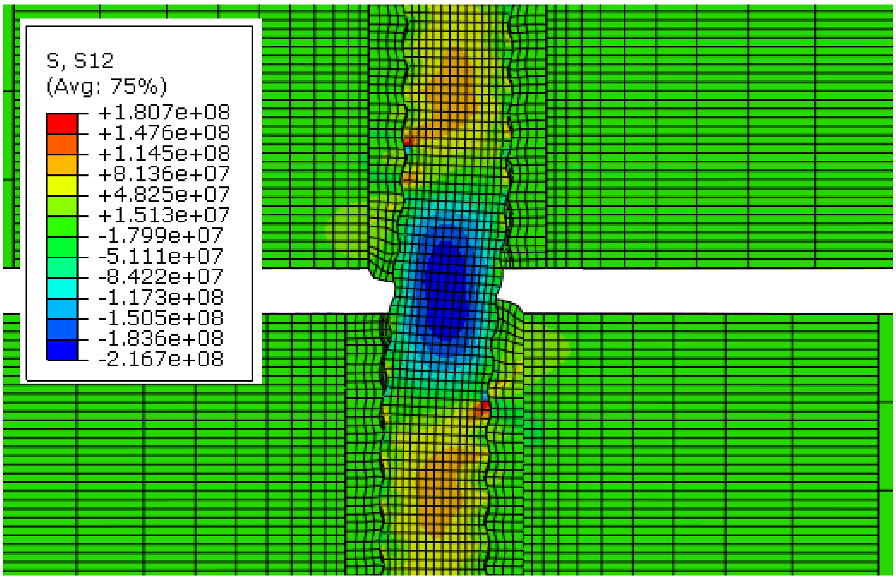

Figure 4.11: Shear stress at 50 degree displacement

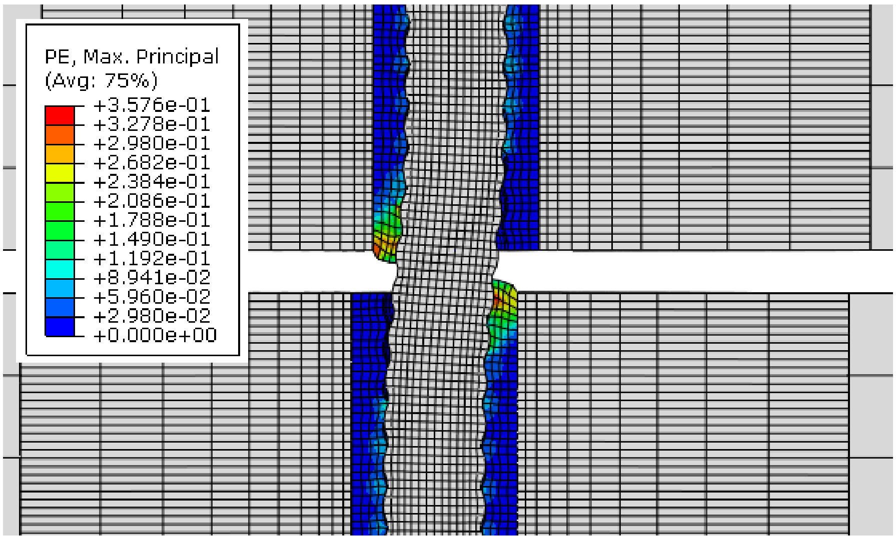

Figure 4.12: Plastic strain at 50 degree displacement

### Stress and Displacement Profiles

The stresses and displacement along the edge and center line is shown for 0°, 50°, 70° and 90° in Figure 4.14. The reported stress profiles has been smoothed, with a moving average, to avoid spikes between the threads and make the patterns more clear. The location of the profiles are marked in Figure 4.13

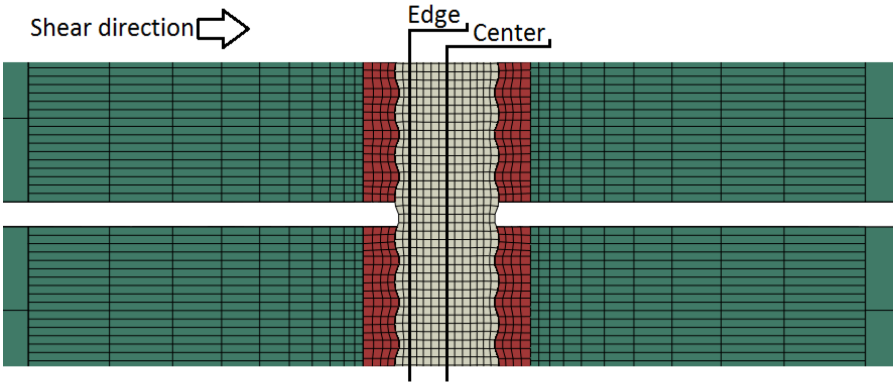

Figure 4.13: Location of the Edge and Center line, used to record data

## 4.6 Discussion and Conclusion

The reported stress profiles in Figure 4.14 Shows how stresses are distributes along the profiles, for 0°, 50°, 70° and 90° displacement angle. At 0° the rock bolt is primarily in tension where the stresses can be seen to be distributed throughout the whole modelled bolt length of 1.2m. As the displacement angle increase it can be observed that the shear stress is becoming more dominant in the center profile, while the axial stresses decrease. For the edge profile it can be seen that that the tensile stresses are concentrated on one side of the joint, where a compression zone is starting to form at displacement angles higher than 45°. The stress profiles at 70° and 90° suggests that the possible causes of failure, is either a combination of shear and tension in the center, pure tension on the edge or a combination of axial compression and shear on the edge. However this model has not represented the test very well in shear and should therefore be used with care.

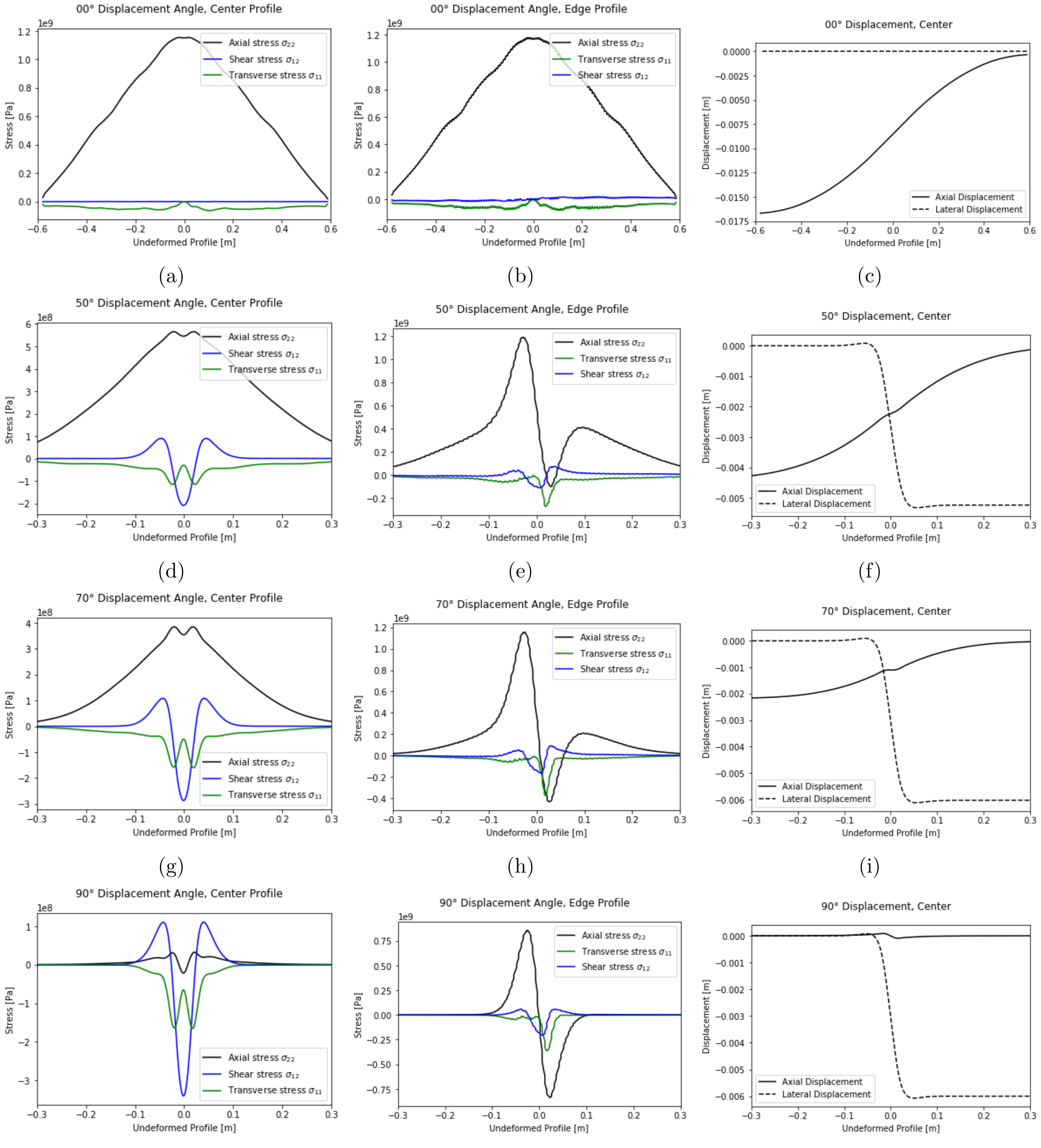

(a) (b) (c)

(d) (e) (f)

(g) (h) (i)

(j) (k) (l)

Figure 4.14: Stress and displacement profiles

# 5 Discussion

A framework has been established to determine the elastic parameters of the Glass Fiber Reinforced Polymer (GFRP) bolt. This has been carried out through experiments and micro mechanical analysis. The experiments involved Optical and SEM microscopy, the matrix burn-off method and tensile testing. All experiments had good agreement between each other, and with fiber stiffness from literature. The optical microscope revealed that the threading had a lower fiber volume fraction, than the core of the bolt. This was disregarded in the report, because it was assumed to have a minor influence on the behaviour of the rock bolt in full scale testing. However, it is likely to be relevant for the load capacity of the nut and faceplate.

The full scale test was carried out using the NTNU bolt rig to simulate different loading conditions. It was found that the strength of the rock bolt at 47° displacement angle was similar to the tensile strength, at 0°, while in the range of 47° to 72° the strength would drop significantly to a value closer to what was measured in pure shear 90°. Furthermore it was seen that the failure patterns would change as the ultimate total load decreased. This is likely an indicator of a change in the stresses that leads to failure.

The numerical model was created to replicate the full scale experiment, but failed to do so, because the model was too simple. The grout was modelled using an elastic brittle Mohr-Coulomb yield criteria, where different parameters were tried in order to find the ones that came closest to describing the grout behaviour. The obtained parameters did seem to describe the tensile behaviour to some degree, but was far from the shear behaviour. A better fit in shear can likely be achieved if element removal is introduced in the material model. However, the grout model might not be the entire explanation of why the model failed to replicate the shear behaviour.

The failure from the FEM model was based on a maximum stress criteria, which caused the bolt to fail in tension from 0° to 70° displacement angle and in shear for 80° and 90°. This failure criteria is likely the strongest way the bolt can be represented, since the bolt is strongest in tension. When comparing the ultimate total loads measured in the model to the full scale experiment, in figure 5.1, it is evident that despite the use of an optimistic failure criteria the bolt model is still acting much weaker than the tested bolt in the experiment.

The reason could be that the bolt is not properly described in the model. The failure in the model happens due to bending of the bolt, causing tensile stress to concentrate. In reality the the matrix might fail along the fibers allowing the fibers to slide along each other, which would cause the tensile stresses to better distribute between the fibers. This could explain how the bolt can maintain such a high strength at a 47° displacement angle. And might also explain drop in stiffness, that has been observed during the shear tests.

It is not obvious how stresses will be distributed in such a model at higher displacement angles and should therefore be simulated to investigate this behaviour.

A way to simulate this in the the finite element model can be to divide the bolt into slices, that are perpendicular to the direction of shear this might also cause the bolt to behave more flexible in shear and allow for larger displacements.

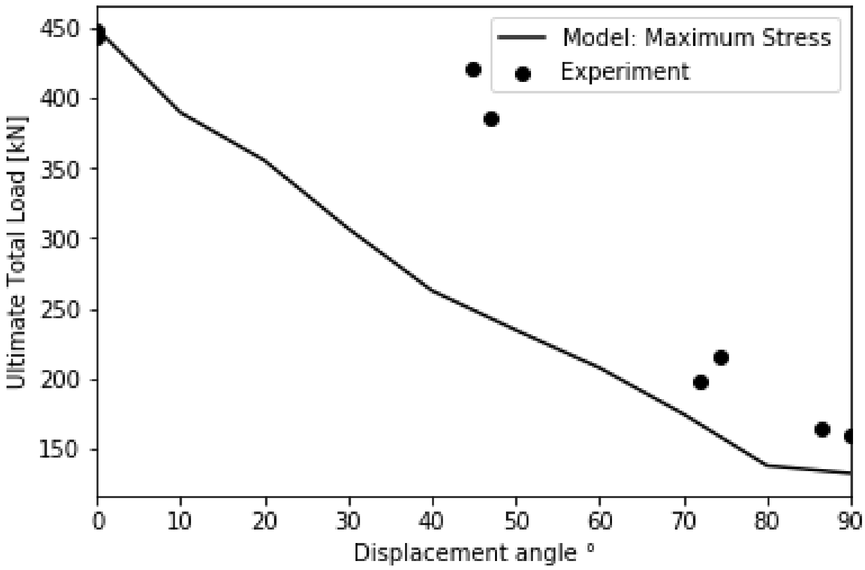

Figure 5.1

Figure 5.2: Ultimate Total Load in relation to displacement angle from FEM, compared to results from experiment

# 6 Conclusion

The elastic properties of the rock bolt has been found through experiments and theory on micro mechanics, where the rock bolt is described as a transverse isotropic material. The estimated value for the tensile stiffness is well documented, while the transverse stiffness and shear modulus are based on a semi-emperical equation, which introduce some uncertainty. The parameters can be found in Table 2.13

The performance of the rock bolt was investigated in 8 full scale tests using the NTNU bolt rig at different load angles, where it was found that the strength of the rock bolt at 47° displacement angle was similar to the tensile strength (0°), while in the range of 47° to 72° the strength would drop significantly to a value closer to what was measured in pure shear (90°). The results from the full scale bolt test can be seen in Tabla 3.3

An attempt to replicate the full scale test was made, using numerical modelling. The model has proven that it is possible to simulate the test rig for large displacements with mechanical interlocking between the bolt and grout, using ABAQUS/-Explicit. However, it was not able to proper simulate the behaviour of the bolt in a combined loading condition and will require further development.

The stresses observed in the numerical model suggest that the observed change in the failure pattern from 47° to 72° displacement angle is caused by a transition from tensile to axial compressive failure. This is however uncertain and should be investigated further.

## 6.1 Recommendation for further work

The research presented in this thesis has led to the following recommendations for further work

- Include element removal in the grout model
- Investigate a better way to accurately simulate the behaviour of GFRP
- Introduce more advanced failure criteria in the model.
- Investigate influence of grout strength and hole diameter on the performance of GFRP bolts

# Bibliography

Abaqus Analysis User's Manual (2010). Version v6.10. *Abaqus Inc*, 2080.

Barbero, E. J. (2017). *Introduction to composite materials design*. CRC press.

Beauson, J., Christensen, J., Andersen, T. L., Madsen, B., and Pedersen, A. (2019). Procedure: Fiber content and porosity analysis of glass fiber composites.

Bjurstrom, S. (1974). Shear strength of hard rock joints reinforced by grouted untensioned bolts. *Proc. 3rd Cong. ISRM, Denver*, 2:1194–1199.

Gilbert, D., Mirzaghorbanali, A., Li, X., Rasekh, H., Aziz, N., and Nemcik, J. (2015). Strength properties of fibre glass dowels used for strata reinforcement in coal mines.

Halpin, J. and Tsai, S. (1967). Environmental factors estimation in composite materials design. *AFML Trans*, pages 67–423.

Hull, D. and Clyne, T. W. (1996). *An introduction to composite materials*. Cambridge university press.

Józefiak, K., Zbiciak, A., Maślakowski, M., and Piotrowski, T. (2015). Numerical modelling and bearing capacity analysis of pile foundation. *Procedia Engineering*, 111:356–363.

Li, C. C. (2017). *Rockbolting: Principles and Applications*. Butterworth-Heinemann.

Li, C. C., Kristjansson, G., and Høien, A. H. (2016). Critical embedment length and bond strength of fully encapsulated rebar rockbolts. *Tunnelling and Underground Space Technology*, 59:16–23.

Snyder, V. W. (1983). Analysis of beam building using fully grouted roof bolts. In *Proc. of the Int. Symp. on Rock Bolting. Rotterdam: Balkema*, pages 187–94.

Stjern, G. (1995). Practical performance of rock bolts. In *Dr.-Ing. thesis*, page 178. Norwegian Institute of Technology Trondheim.

Thomas, A. (2018). Glass fibre reinforced plastic (gfrp) permanent rockbolts.

# Appendices

# A Full scale test

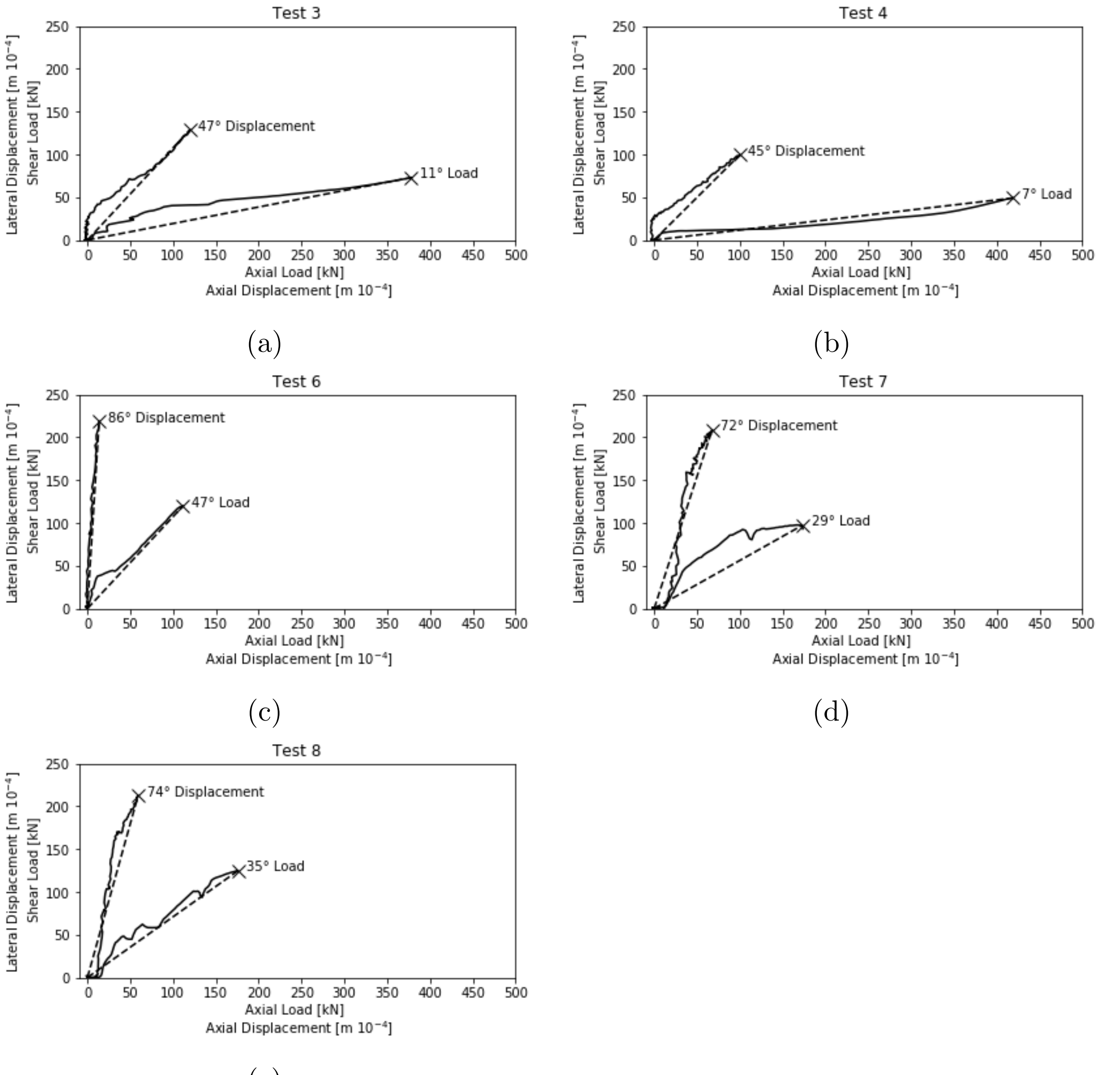

(a) (b)

(c) (d)

(e)

Figure A.1

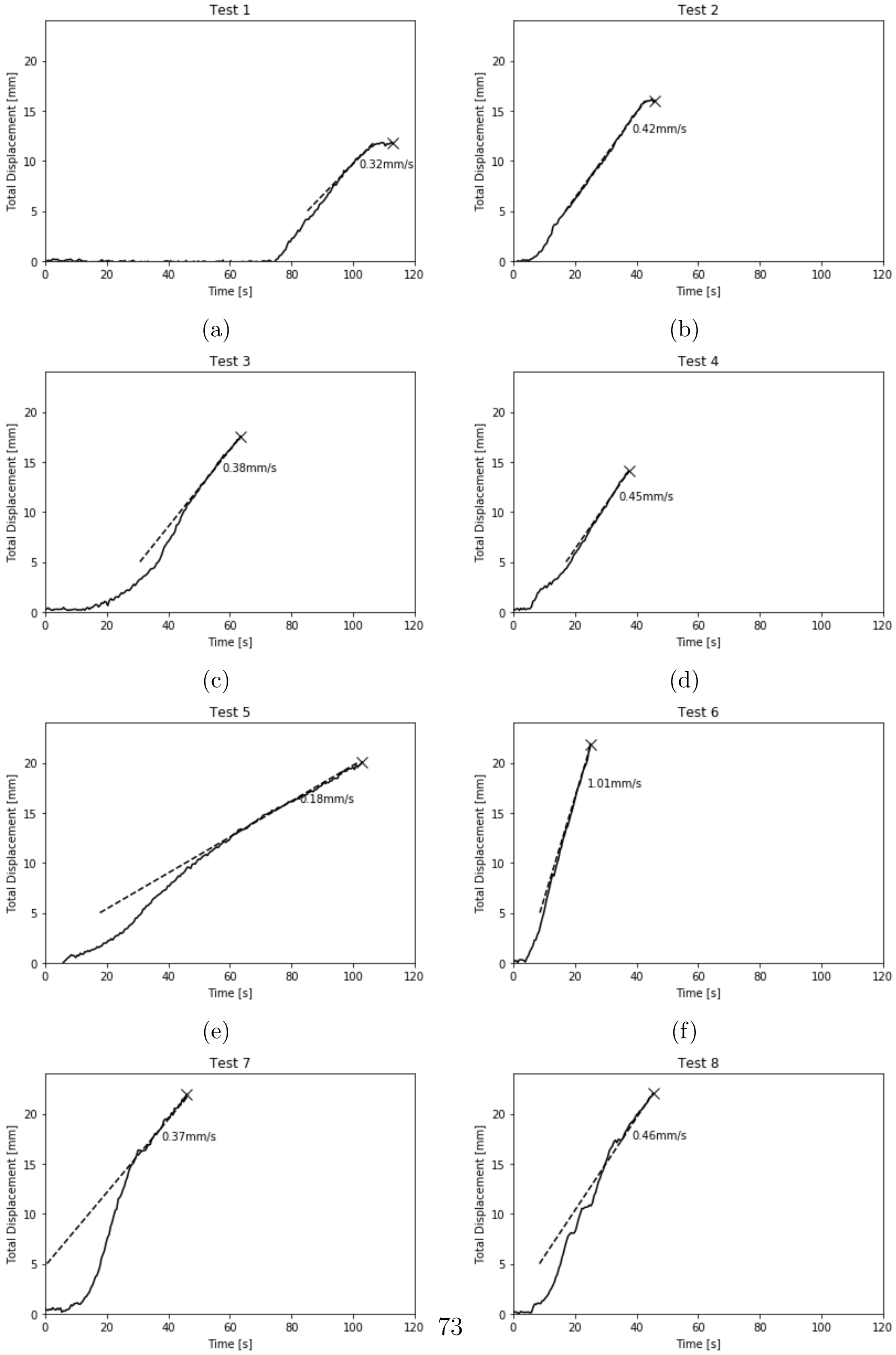

(a) (b)

(c) (d)

(e) (f)

(g) (h)

Figure A.2

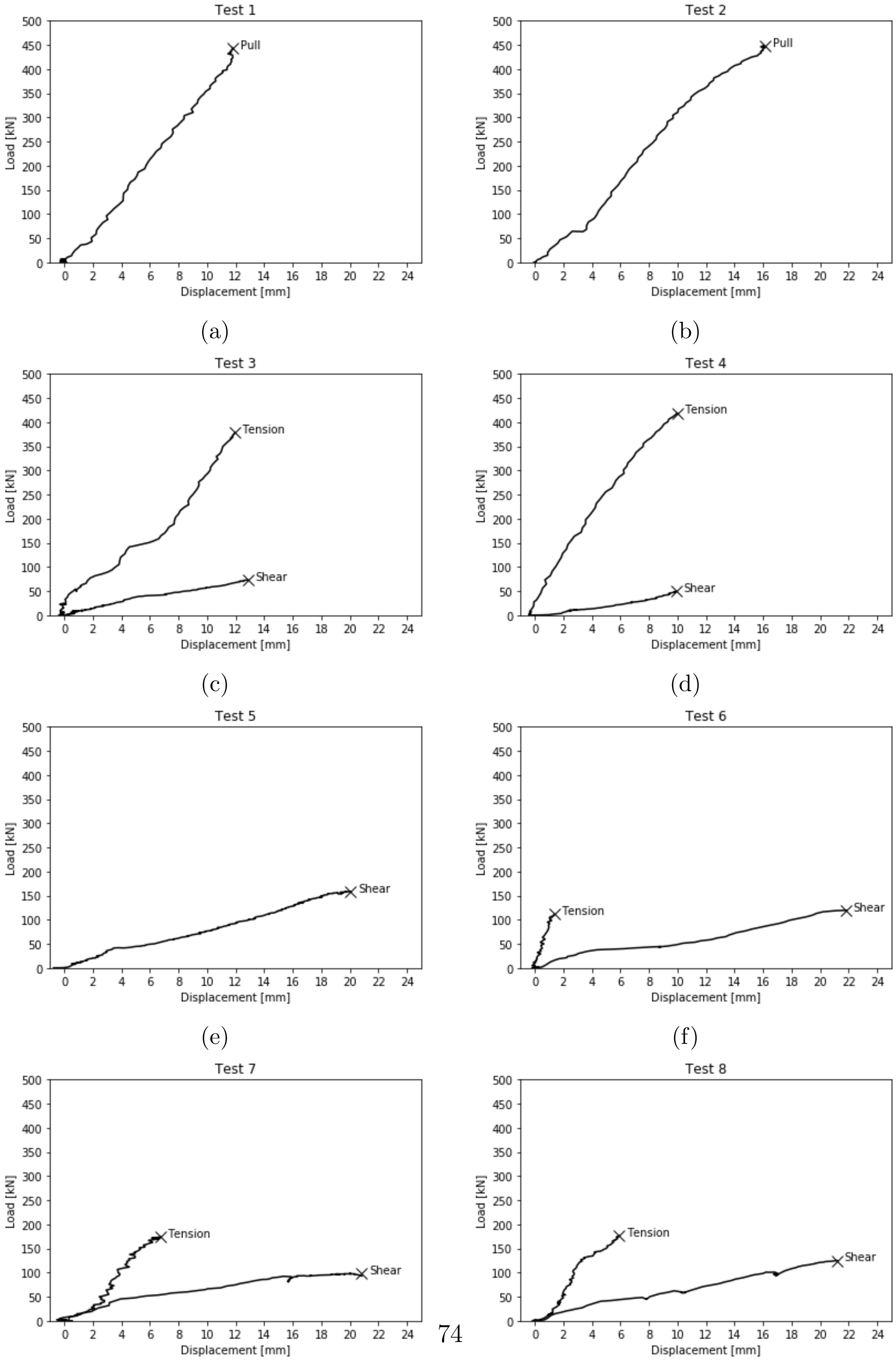

(a) (b) (c) (d) (e) (f) (g) (h)

Figure A.3

# B FEM results

## B.1 0 degrees

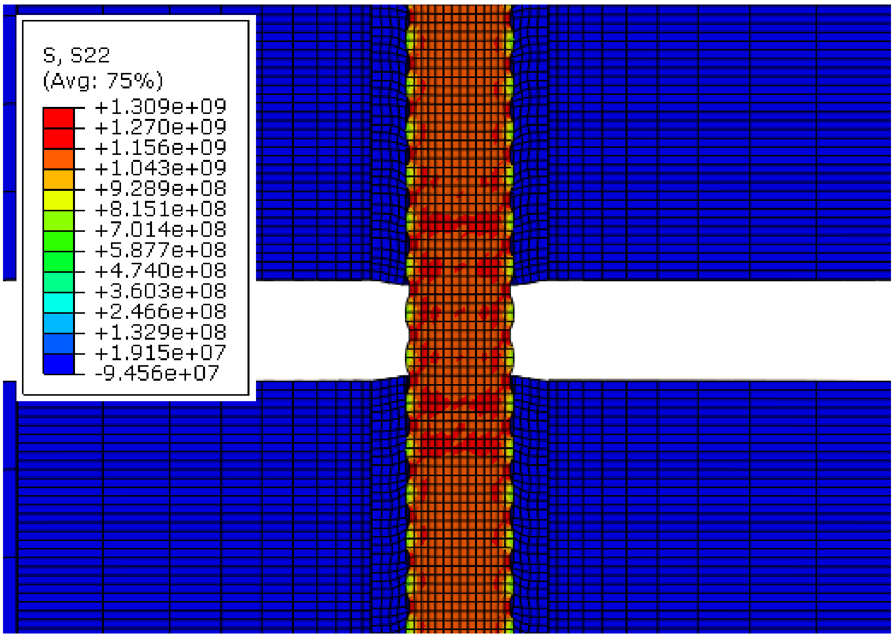

Figure B.1: Axial stresses at 0 degree displacement

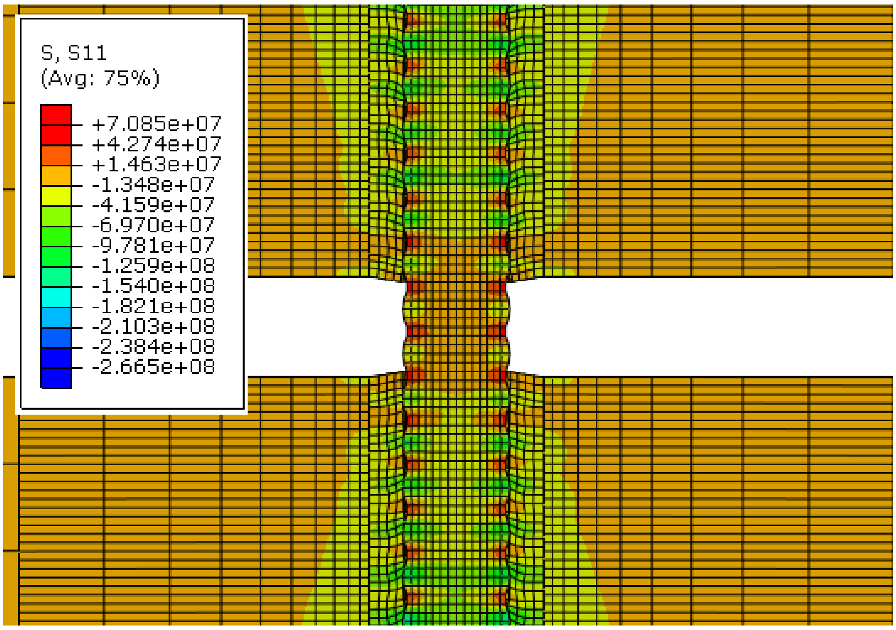

Figure B.2: Transverse stressse at 0 degree displacement

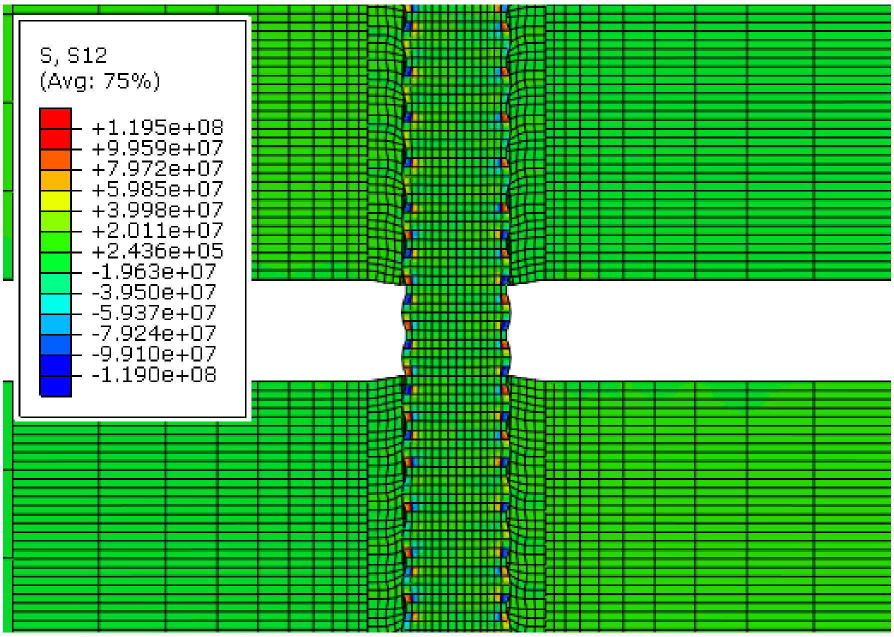

Figure B.3: Shear stresses at 0 degree displacement

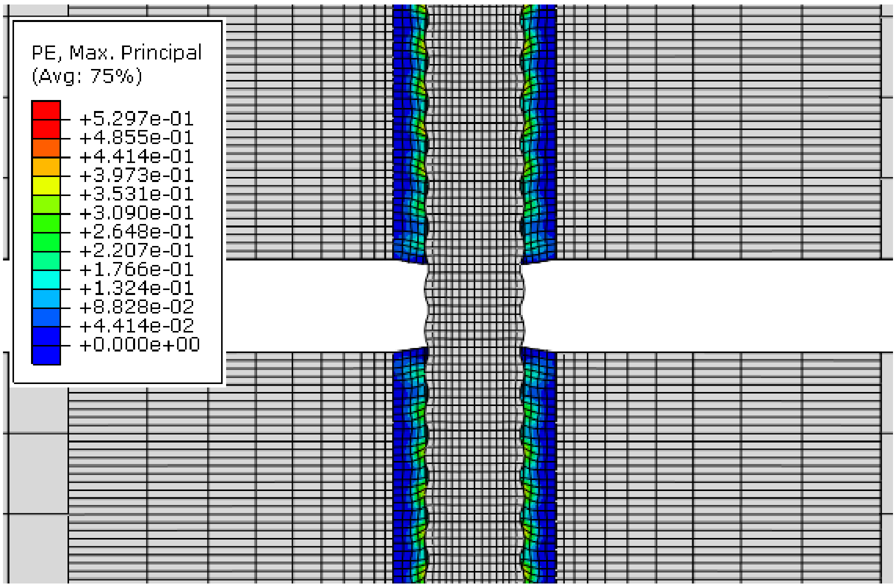

Figure B.4: Plastic strain at 0 degree displacement

## B.2 50 degrees

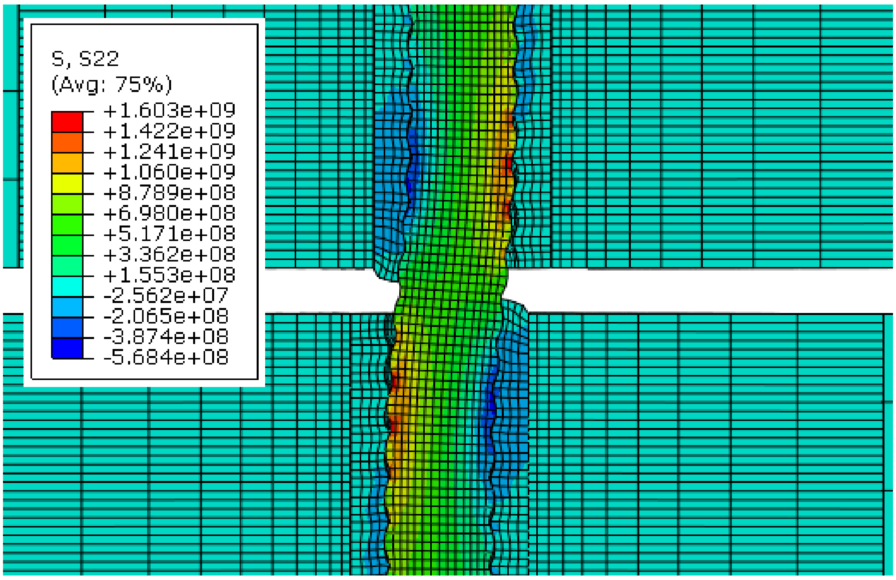

Figure B.5: Axial stresses at 50 degree displacement

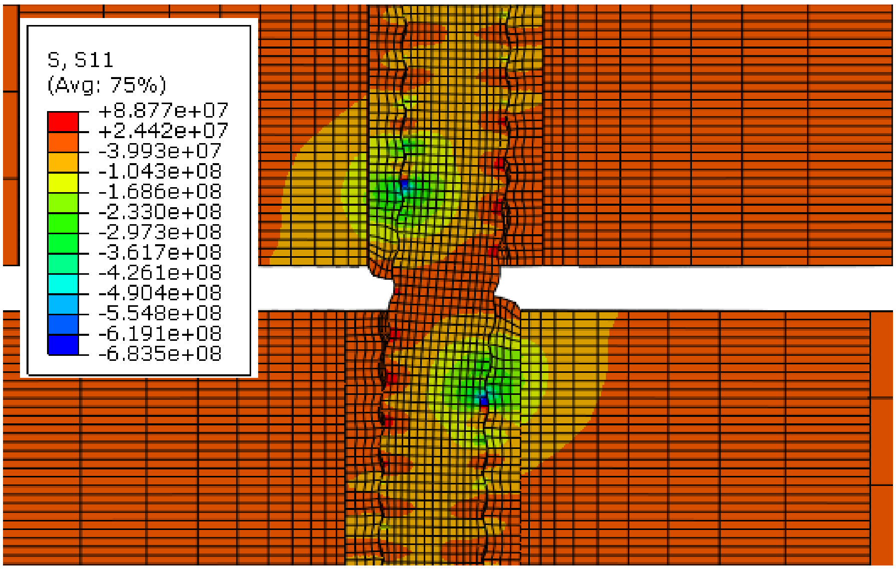

Figure B.6: Transverse stresses at 50 degree displacement

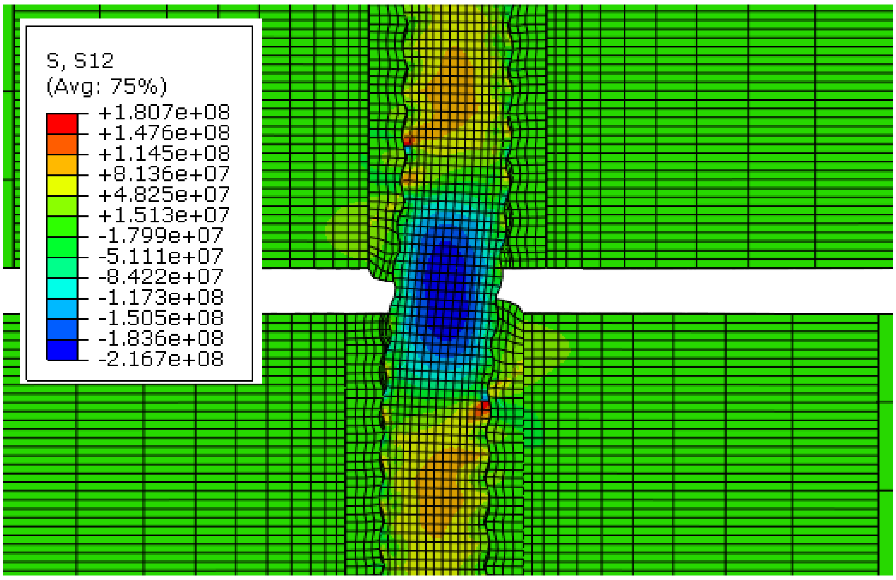

Figure B.7: Shear stresses at 50 degree displacement

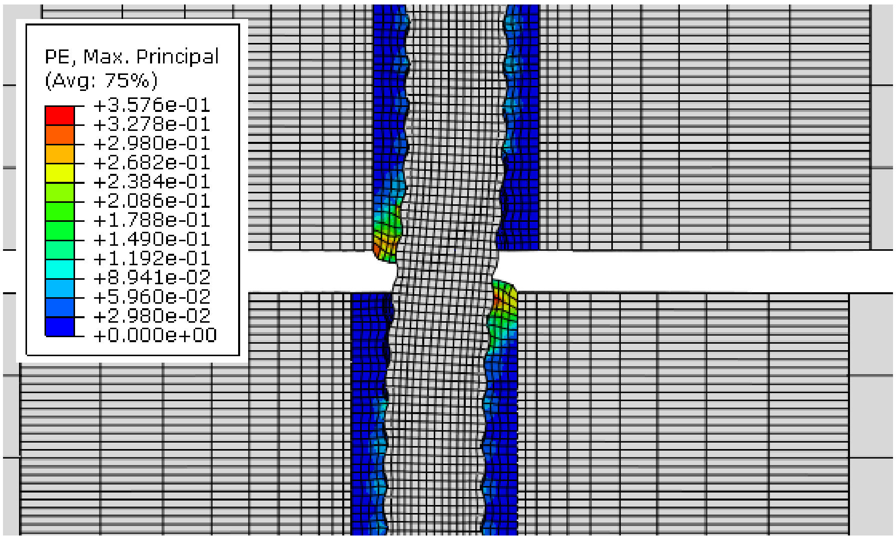

Figure B.8: Plastic strain at 50 degree displacement

## B.3 90 degrees

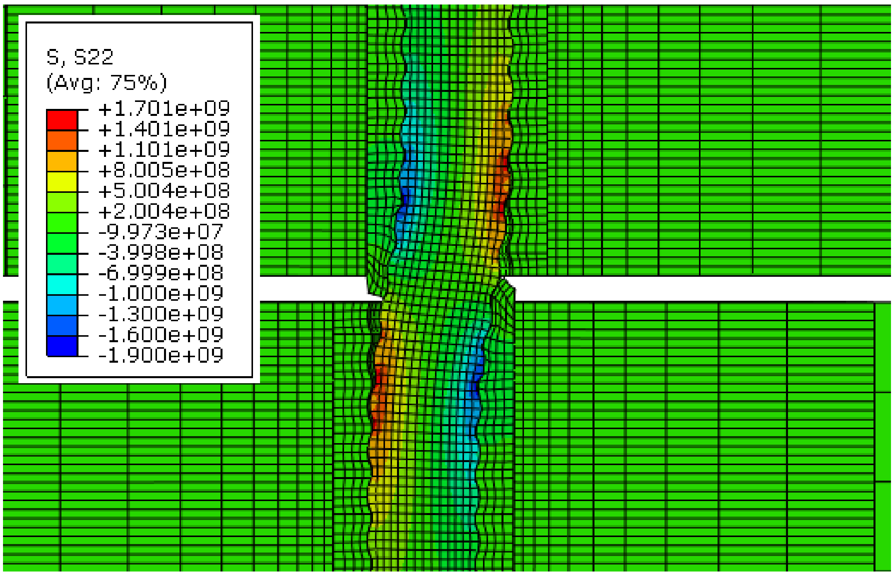

Figure B.9: Axial stress at 90 degree displacement

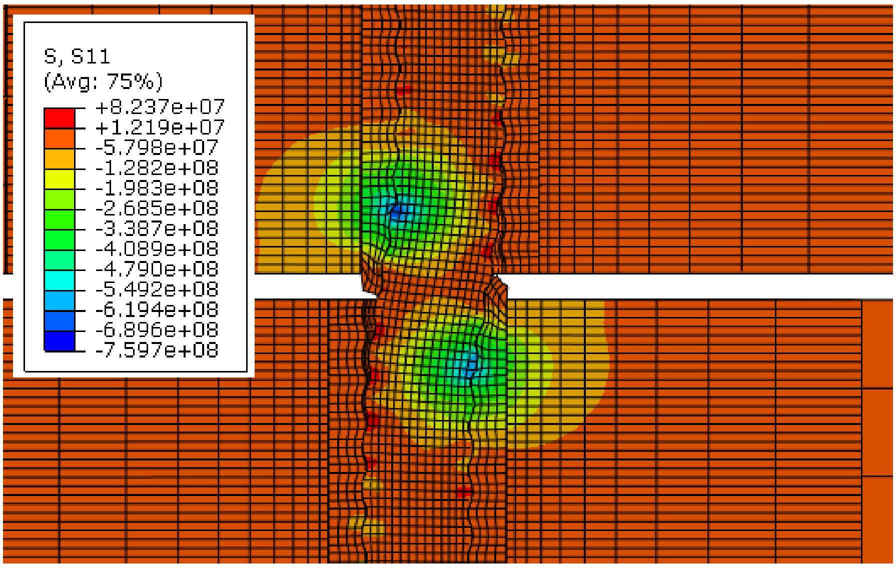

Figure B.10: Transverse stresses at 90 degree displacement

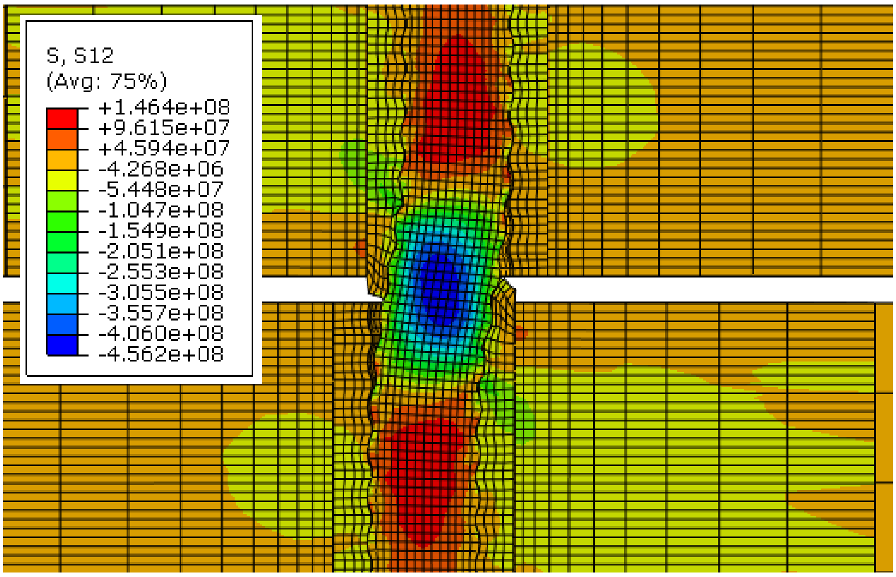

Figure B.11: Shear stresses at 90 degree displacement

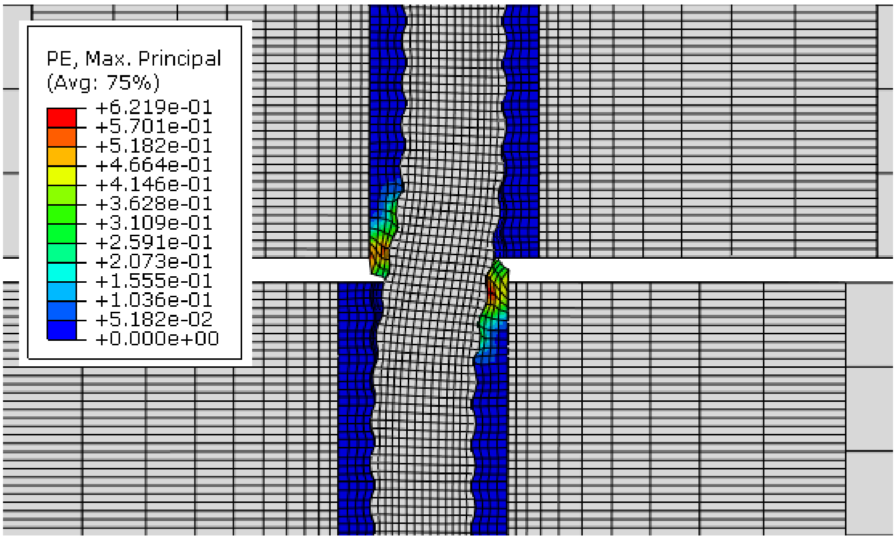

Figure B.12: Plastic strain at 90 degree displacement